HYPERSONIC HEAT TRANSFER LOAD ANALYSIS IN STAR-CCM+

A Thesis

presented to

the Faculty of California Polytechnic State University,

San Luis Obispo

In Partial Fulfillment

of the Requirements for the Degree

Master of Science in Aerospace Engineering

by

Robert Jin Comstock

December 2020

COMMITTEE MEMBERSHIP

TITLE: Hypersonic Heat Transfer Load Analysis in STAR-CCM+

AUTHOR: Robert Jin Comstock

DATE SUBMITTED: December 2020

COMMITTEE CHAIR: Dianne DeTurris, Ph.D.
Professor, Aerospace Engineering

COMMITTEE MEMBER: Paulo Iscold, Ph.D.
Professor, Aerospace Engineering

COMMITTEE MEMBER: Aaron Drake, Ph.D.
Professor, Aerospace Engineering

COMMITTEE MEMBER: Kim Shollenberger, Ph.D.
Professor, Mechanical Engineering

ABSTRACT

Hypersonic Heat Transfer Load Analysis in STAR-CCM+

Robert Jin Comstock

This thesis investigates the capabilities of STAR-CCM+, a Computational Fluid Dynamics (CFD) software owned by Siemens, in predicting hypersonic heat transfer loads on forward-facing surfaces. Results show that STAR-CCM+ predicted peak heat transfer loads within $\pm 20\%$ of experimental data on the leading edge of a delta wing design from the X-20 Dyna-Soar program with 73° of sweep. Steady-state laminar simulations were run as replications of wind tunnel tests documented in NASA CR-535, a NASA technical report that measured and studied the hypersonic pressure and heat transfer loads on preliminary X-20 wing designs across a wide range of Reynolds numbers and Mach numbers in different wind tunnel and shock tunnel facilities. One of the Mach 8.08 test cases that was run at NASA Arnold Engineering Development Center Wind Tunnel B was selected as the case of comparison for this thesis, which was designated as test AD462M-1 in the original report. The CFD simulations assumed an ideal gas in laminar flow with temperature-dependent viscosity, thermal conductivity, and isobaric specific heat across an angle of attack range from 0° to 30°. A separate CFD study of heat transfer loads of a hemisphere-cylinder at Mach 6.74 was used as a simpler and less computationally-expensive validation case compared against wind tunnel data from NASA Langley Research Center to help select the appropriate CFD solver and mesh settings for this thesis.

For the hemisphere-cylinder, the heat transfer load at the stagnation point was overpredicted in STAR-CCM+ by 21.8%. Peak heat transfer loads on the delta wing leading edge were all within $\pm 20\%$ of the wind tunnel data, which was published for angles of attack between 15° to 30°. A more adverse heat transfer gradient along the leading edge of the delta wing was also observed in the direction from the front of the wing to the outer

wing tip when compared to wind tunnel data. The pressure loads on the delta wing leading edge in CFD were within $\pm 10\%$ of wind tunnel measurements.

ACKNOWLEDGMENTS

I would like to thank the committee chair Dr. DeTurris for her teachings and oversight in both technical and social skills she has taught me, all the way from the first lecture I had from her to my final months of school while writing this thesis. I appreciate the valuable feedback and oversight you provided and I will retain and apply this knowledge well into my professional career.

Thank you to the other committee members as well, Dr. Iscold, Dr. Drake, and Dr. Shollenberger for helping me build the scope of my thesis by providing very constructive feedback during the proposal and defense stages of this thesis.

I want to thank my family, Sam, Kate and Will Comstock for supporting me all the way. I would like to dedicate this work to you for all the ongoing support you gave during my studies and activities outside the classroom. I definitely would not have reached this point in my education without your help.

I would also like to thank my fellow classmates for all the academic support in class, Kendra Bubert for helping with curriculum selection and logistics, and Brandon Goddard for providing technical support for remotely using the Bishop cluster during the COVID-19 pandemic.

TABLE OF CONTENTS

LIST OF TABLES

LIST OF FIGURES

NOMENCLATURE

a	Polynomial Coefficient
b	Quarter of Diameter
c_p	Isobaric Specific Heat
$c_{p\infty}$	Freestream Isobaric Specific Heat
c_v	Isochoric Specific Heat
$c_{v\infty}$	Freestream Isochoric Specific Heat
C_f	Skin Friction Coefficient
C_p	Pressure Coefficient
D	Diameter
h	Heat Transfer Coefficient
h_c	Convective Heat Transfer Coefficient
k	Thermal Conductivity
k_{ref}	Reference Thermal Conductivity
k_∞	Freestream Thermal Conductivity
k_σ	Thermal Conductivity Behind a Normal Shock
L	Delta Wing Body Length
L_{Ref}	Reference Length
M_∞	Freestream Mach Number
M_σ	Mach Number Behind a Normal Shock
Nu	Nusselt Number
p	Pressure
p_o	Stagnation Pressure
p_s	Local Static Pressure
p_∞	Freestream Static Pressure
p_σ	Static Pressure Behind a Normal Shock

$\dot{q}$	Heat Transfer Rate
R	Gas Constant
Re	Reynolds Number
Re_D	Reynolds Number with Respect to Diameter
Re_x	Local Reynolds Number
Re_σ	Reynolds Number Behind a Normal Shock
S	Sutherland Temperature
St	Stanton Number
St_o	Reference Stanton Number
T	Temperature
T_i	Initial Wind Tunnel Model Temperature
T_f	Air Temperature
T_{max}	Maximum Temperature
T_{min}	Minimum Temperature
T_o	Stagnation Temperature
T_w	Surface Temperature
T_σ	Static Temperature Behind a Normal Shock
u_{fric}	Shear Velocity
u_∞	Freestream Velocity
$u+$	Non-dimensional Velocity in Boundary Layer
x	Position Along a Surface
y	Height in Boundary Layer
$y+$	Non-dimensional Height in Boundary Layer
δ	Boundary Layer Height
γ	Ratio of Specific Heats
μ	Viscosity
μ_{ref}	Reference Viscosity

μ_∞	Freestream Viscosity
μ_σ	Viscosity Behind a Normal Shock
ρ	Density
ρ_∞	Freestream Density
ρ_σ	Density Behind a Normal Shock
τ_{Wall}	Shear Stress
$\theta_{Surface}$	Local Surface Angle of Incidence

Chapter 1

INTRODUCTION

Chapter 1 of this thesis covers the concepts and governing equations that pertain to hypersonic loads. The history of how re-entry became a subject of interest in the aerospace industry is covered in Section 1.1. Section 1.2 covers the fundamental equations necessary for calculating hypersonic pressure and heat transfer loads. The Computational Fluid Dynamics (CFD) software that was used to run the simulations for this thesis is introduced in Section 1.3 along with the governing equations that are utilized. Section 1.4 provides an overview of the ideal gas model and the relevant governing equations that are utilized by the CFD software.

1.1 Introduction to Re-Entry

Re-entry refers to the stage at which an object in space that has left a planet's atmosphere starts to re-enter the same atmosphere. This is what happens to spacecraft that are launched into orbit and eventually fall back to earth once they are no longer used. A more familiar but re-usable example to some of us is the space shuttle. The space shuttle would be launched into orbit with a rocket booster and then re-enter the Earth's atmosphere to perform a landing maneuver onto a runway.

The subject matter of how air behaves around a spacecraft during re-entry became a growing interest during the early stages of the cold war during the space race, which was between the United States and the Soviet Union after World War II. The first missions to send humans into space entailed sending astronauts into orbit by containing them in small spacecraft called space capsules. The space capsules were each launched into orbit

with a rocket, and the capsule would eventually re-enter the earth's atmosphere. This was how the Apollo missions to the moon were accomplished by sending astronauts to and from space. An artist's painting of one the Apollo capsules performing a re-entry maneuver is shown in Figure 1.1.

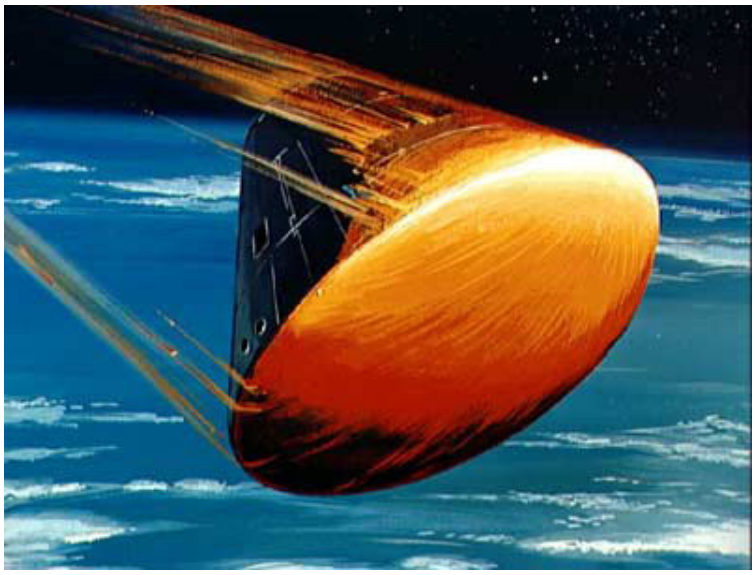

Figure 1.1: Artist's painting of the Apollo capsule re-entering Earth's atmosphere [1].

Spacecraft that are designed to go into space and eventually return to Earth usually travel several kilometers per second when in orbit. When a spacecraft begins re-entering the atmosphere, it undergoes very high pressure loads and high aerothermodynamic loads, which refers to the heat transfer loads caused by the presence of high temperature gases in front of the spacecraft. This happens when the air hitting the spacecraft during re-entry compresses and undergoes a very large rise in temperature. For reference as to how hot this gas can get, some regions of the compressed air in front of the spacecraft can reach temperatures higher than the surface of the sun [2].

To characterize when a spacecraft will be undergoing very high pressure and heat transfer loads, the Mach number is one of the primary performance parameters of interest. It is typical for some spacecraft to be traveling well above Mach 20 during re-

entry. Any object traveling faster than Mach 5 is considered to be traveling at hypersonic speed [2].

The earliest manned flights at hypersonic speeds were done with the X-15, an experimental space plane that reached Mach 6.7 to gather valuable hypersonic test flight data prior to the US space programs [3]. The first space programs became the foundation for the iconic space shuttle that a lot of us may be familiar with today, despite the fact that it is now retired.

While the space shuttle was well-known for its ability to be sent into space and back multiple times, there were actually a lot of other spacecraft and shuttle concepts that were being pursued during the cold war that never got built. Some of these concepts went far enough into the design process to undergo rigorous research and development, including wind tunnel testing. Despite these concepts not making it to operational status, the research and development that went into some of these designs was used to support the final design of the space shuttle that was actually built and flown [4]. Some of these concepts are shown in Figure 1.2 below.

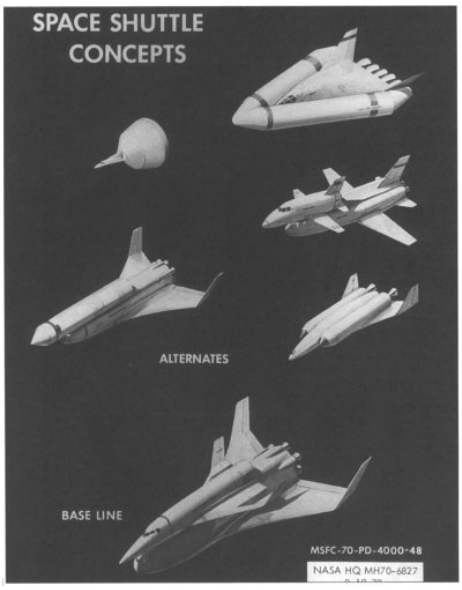

Figure 1.2: Early space shuttle concepts [5].

One of these earlier concepts that never made it to operational status was the X-20 Dyna-Soar, which was effectively a small-scale space shuttle. It was designed for military applications in space, but cost issues led to the program's cancellation. Fortunately, the research and development from the program proved to be useful for the development of the space shuttle [4]. Some of the data that went into this work is publicly available online on the NASA Technical Reports Server (NTRS). This includes hypersonic wind tunnel and shock tunnel test data from NASA-CR-535, a NASA technical report titled "Analysis of hypersonic pressure and heat transfer tests on delta wings with laminar and turbulent boundary layers" [6]. The data in this report was utilized for validating the hypersonic CFD simulations that were run in this thesis. Chapter 4 will cover the specifics of the background and data from NASA-CR-535. An artist's painting of the X-20 Dyna-Soar is shown in Figure 1.3.

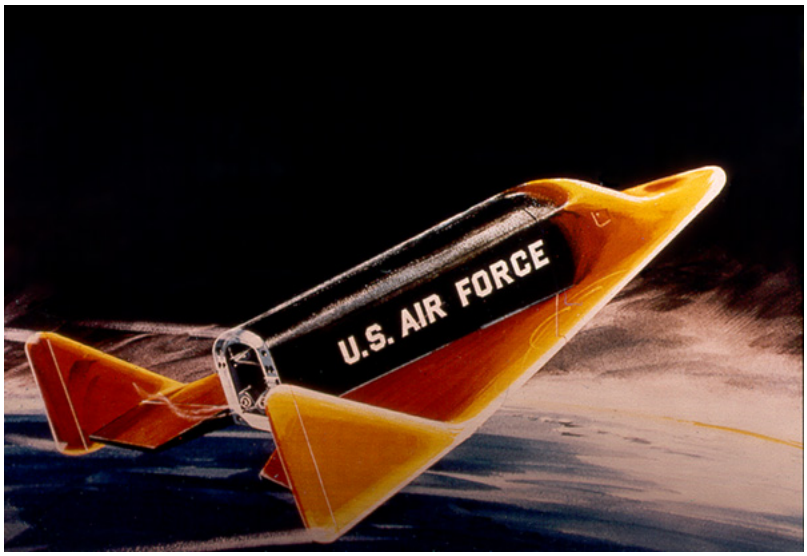

Figure 1.3: Artist's painting of the X-20 Dyna-Soar [7].

1.2 Hypersonic Load Equations

The pressure and heat transfer loads that a spacecraft undergoes while traveling at hypersonic speeds need to be predicted and quantified in very specific locations. The surfaces

that face the direction of incoming flow are usually where the highest loads are, which ultimately drives the design of the underlying spacecraft material and structure in these regions. Using the space shuttle as an example, this would be right at the leading edge of the wings and the tip of the nose.

These loads are typically predicted on scale models of spacecraft in wind tunnel tests. To make these loads comparable between different scales of the spacecraft, they must be modified into a non-dimensional form, which means to have no units. This means that the loads measured from scale wind tunnel models can be ultimately converted into full-scale loads for a real spacecraft based on it's full-scale conditions.

For measuring pressure, the pressure coefficient (C_p) is a non-dimensional pressure value anywhere in a flow field. This is defined as the difference in local static pressure (p_s) and freestream static pressure (p_∞) divided by the dynamic pressure of the freestream, which is a function of freestream density (ρ_∞) and velocity (u_∞). The equation for pressure coefficient is shown in Equation 1.1 below. It is applicable for quantifying pressure loads at both low and high Mach numbers.

$$C_p = \frac{p_s - p_\infty}{\frac{1}{2}\rho_\infty {u_\infty}^2} \tag{1.1}$$

Pressure coefficient can be measured on the surface of an object to know what pressure load is locally imparted. It is very dependent on three-dimensional (3D) effects, which are a function of the flow field conditions as well as the geometry of the object. The static pressure can be measured using a pressure sensor, which is usually a pressure transducer, that is connected to a tubular hole in the object's surface called a pressure tap. If the freestream static pressure, density and velocity are known with a pressure measurement, the pressure coefficient can be calculated.

For hypersonics however, the pressure coefficient on an object's surface can actually be estimated with a simple algebraic relation. The relation assumes that the pressure coefficient (C_p) anywhere on a surface that is facing the incoming hypersonic flow is a function of the surface's local angle of incidence relative to the incoming flow ($\theta_{Surface}$). Any surface that is not directly facing the freestream, or is in what is referred to as the shadow region, has a pressure coefficient of 0. This is represented in Equation 1.2 with also a visual example in Figure 1.4. The concept is referred to as Newtonian Theory for hypersonics, hence being conceptualized by Newton. Newton originally created this concept for low speed flow but it ended up being valid many years later for hypersonics. The methodology of predicting pressure loads assuming Newtonian Theory has proven to be a very accurate approach for designing spacecraft that travel at hypersonic speeds. This was actually the approach utilized in the development process of the X-15 and space shuttle for estimating pressure loads [2].

$$C_p = 2sin^2\theta_{Surface} \tag{1.2}$$

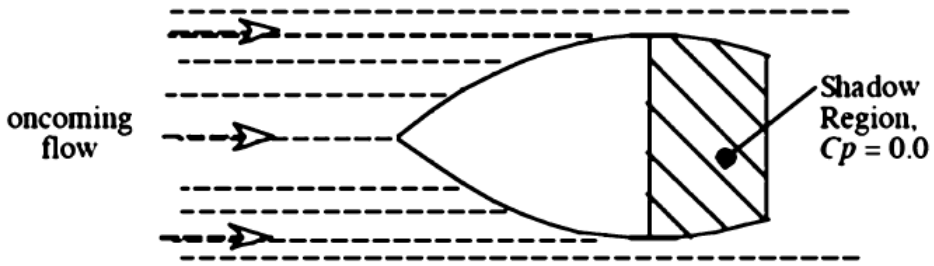

Figure 1.4: An object in hypersonic flow with the shadow region specified where the pressure coefficient is 0 [2].

Heat transfer loads in hypersonic flow can't be modeled with a concept as simple as Newtonian Theory. Not only are they very dependent on freestream conditions, 3D flow field effects, and the geometry of the object in hypersonic flow, but they are also dependent on a thin layer of slow-moving air on the surface of the object called the boundary

layer. A boundary layer exists on any surface that has relative motion to a viscous fluid around it. When the direction of the flow within the boundary layer is predominantly parallel to the surface it is attached to, it is in a laminar state. When the fluid velocity in the boundary layer is no longer parallel to the surface it's traveling along, small swirls of fluid called eddies form and the boundary layer is now in a turbulent state. A boundary layer that is traveling along a surface and is initially laminar can eventually transition into a turbulent state. To predict this transition state, the inertial forces are quantified by the product of freestream density (ρ_∞), velocity (u_∞) and a reference length (L_{Ref}) and then divided by the freestream viscosity (μ_∞). This ratio is referred to as the Reynolds number (Re). This is shown in Equation 1.3 in the form of local Reynolds number (Re_x) because the reference length is defined as the position along a surface (x). When the Reynolds number is generally above 5×10^5 at a certain position along a surface, the boundary layer starts to transition into a turbulent state. Figure 1.5 shows a graphical representation of a laminar boundary layer transitioning to a turbulent one.

$$Re_x = \frac{\rho_\infty u_\infty x}{\mu_\infty} \tag{1.3}$$

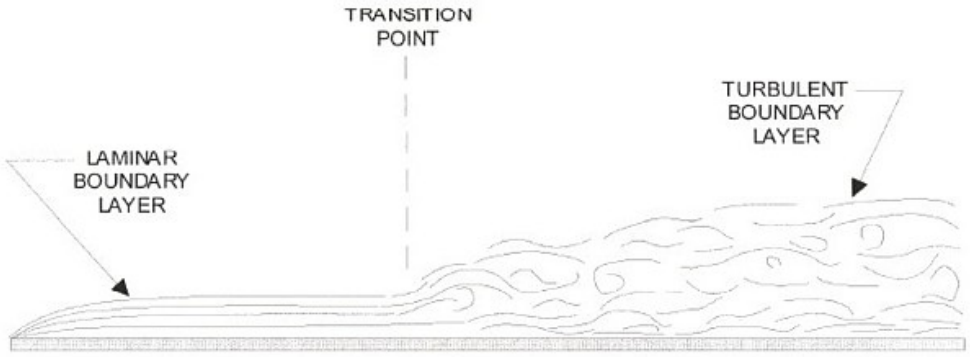

Figure 1.5: A boundary layer over a flat plate becoming turbulent from a laminar state [8].

This is very important for heat transfer in hypersonics because a turbulent boundary layer transfers more heat to the surface it is in contact with than a laminar boundary layer [2].

To quantify the heat transfer loads between a surface and a fluid such as hot air around an object in hypersonic flow, a dimensional coefficient called the heat transfer coefficient (h) can be referenced. This is generally defined as the heat transfer rate ($\dot{q}$) between the air and the surface divided by the difference in air temperature (T_f) and surface temperature (T_w), shown in Equation 1.4 below.

$$h = \frac{\dot{q}}{T_f - T_w} \tag{1.4}$$

The heat transfer coefficient on the surface of an object in hypersonic flow can be calculated if the heat transferred and the temperature difference is known. One way to create a non-dimensional quantity of heat transfer is to divide the heat transfer coefficient (h) by the freestream's thermal capacity as a function of freestream density (ρ_∞), velocity (u_∞) and isobaric specific heat ($c_{p\infty}$). This is referred to as the Stanton number (St) in Equation 1.5.

$$St = \frac{h}{\rho_\infty u_\infty c_{p\infty}} \tag{1.5}$$

Another non-dimensional form of measuring heat transfer is Nusselt number (Nu), which is the ratio of convective heat transfer to conductive heat transfer. It is defined as the convective heat transfer coefficient (h_c) times a reference length (L_{Ref}) divided by the freestream thermal conductivity (k_∞), shown in Equation 1.6.

$$Nu = \frac{h_c L_{Ref}}{k_\infty} \tag{1.6}$$

The importance of using both Stanton number and Nusselt number comes into play when analyzing the results of hypersonic wind tunnel tests. They can be calculated by measuring the local surface temperatures on a wind tunnel model surface over time, from which the dimensional heat transfer coefficients can be calculated. From here, the non-dimensional Stanton number and Nusselt number can be calculated and used to predict full-scale heat transfer loads for a full-scale spacecraft.

1.3 CFD Governing Equations

CFD is a tool used for predicting the flow field around an object through numerical means. This is done with computer software that breaks up the overall fluid volume into smaller discrete volumes called cells. The fluid properties such as pressure, velocity, and density are calculated at each cell. This discretized collection of cells is called a mesh. The CFD software that is used in this thesis is STAR-CCM+, a commercial software owned by Siemens. STAR-CCM+ can simulate a very wide range of flow regimes. It is extensively used for low speed studies such as flow fields around aircraft, ground vehicles, and even internal fluids, but it can also be used for hypersonic scenarios as well. For this thesis, STAR-CCM+ version 15.02.007 was utilized. Figure 1.6 has two examples of low speed scenarios that can be simulated for an airplane and a Formula 1 vehicle.

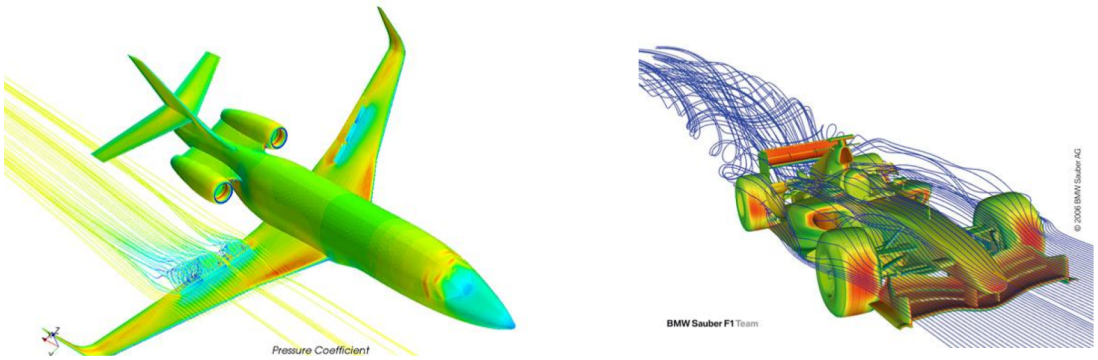

Figure 1.6: Example CFD simulations in STAR-CCM+ [9][10].

CFD is governed by the Navier Stokes equations, which are based on the laws of physics that define the conservation of mass, momentum, and energy. They can take into account both viscous and compressibility effects, both of which are necessary to predict loads in hypersonics. Equation 1.6 is for conservation of mass which defines the sum of the time derivative of density and the divergence of momentum to be 0. Also shown below, Equation 1.7 is for the conservation of momentum, which is defined as the inertia per volume equal to the sum of the pressure gradient, viscous diffusion, and external forces. Both equations are shown in compact vector form.

$$\underbrace{\frac{\partial \rho}{\partial t}}_{\substack{\text{Time derivative} \\ \text{of density}}} + \underbrace{\nabla \cdot (\rho \vec{u})}_{\substack{\text{Divergence of} \\ \text{momentum}}} = 0 \tag{1.6}$$

$$\underbrace{\rho \frac{D\vec{u}}{Dt}}_{\substack{\text{Inertia per} \\ \text{volume}}} = \underbrace{-\nabla p}_{\substack{\text{Pressure} \\ \text{gradient}}} + \underbrace{\mu \nabla^2 \vec{u}}_{\substack{\text{Viscous} \\ \text{diffusion}}} + \underbrace{\rho \vec{g}}_{\substack{\text{External} \\ \text{forces}}} \tag{1.7}$$

The full form of the equations are time-dependent, meaning that they can predict the quantities of the flow field as a function of time. This however can be simplified by removing the time dependent terms. To predict steady turbulent flow, the variables are time averaged with fluctuation terms. This reduces the equations to the Reynolds-Averaged

Navier Stokes (RANS) equations. Equation 1.8 is the momentum equation in RANS form in indicial notation, represented as the terms of convection equal to the sum of the pressure gradient and the laminar and turbulent stresses. The turbulent stresses must be calculated with a turbulence model, such as the k-ω SST model.

$$\underbrace{\frac{\partial}{\partial x_j}(\rho\overline{u_i}\,\overline{u_j})}_{\text{Convection}} = \underbrace{\frac{\partial \overline{p}}{\partial x_i}}_{\substack{\text{Pressure}\\ \text{gradient}}} + \frac{\partial}{\partial x_j}\left[\underbrace{\mu\left(\frac{\partial \overline{u_i}}{\partial x_j} + \frac{\partial \overline{u_j}}{\partial x_i}\right)}_{\substack{\text{Laminar}\\ \text{stresses}}} - \underbrace{\rho\overline{u_i' u_j'}}_{\substack{\text{Turbulent}\\ \text{stresses}}}\right] \tag{1.8}$$

To ensure that viscous effects are properly accounted for in CFD, very thin cells called prism layers in STAR-CCM+ are placed around surfaces that have a boundary layer forming over them. This is because in a boundary layer, whether it's turbulent or laminar, there is a large velocity gradient in the direction normal to the surface that the boundary layer is attached to. The velocity profile that is present in a turbulent boundary layer can be predicted and modeled along a surface in a non-dimensional form called the law of the wall. In general for turbulent boundary layers in CFD, it is important that the first prism layer cell on a surface is small enough such that it is within the laminar sublayer where non-dimensional velocity ($u+$) is equal to non-dimensional height ($y+$) and the physical prism layer height equates to a $y+$ value that is no larger than 1. This laminar sublayer that must be modeled is beneath the logarithmic region of the non-dimensional profile. The $y+$ value at the first prism layer cell is evaluated by the CFD software based on the fluid conditions near the surface. The growth rate at which the prism layers are grown outward is measured by how much larger in height the next layer is relative to the previous one, which is generally accepted to be 1.2. The law of the wall model with it's logarithmic section and laminar sublayer is labeled in Figure 1.7 along with a visual reference of a prism layer surface mesh grown off of a surface in STAR-CCM+.

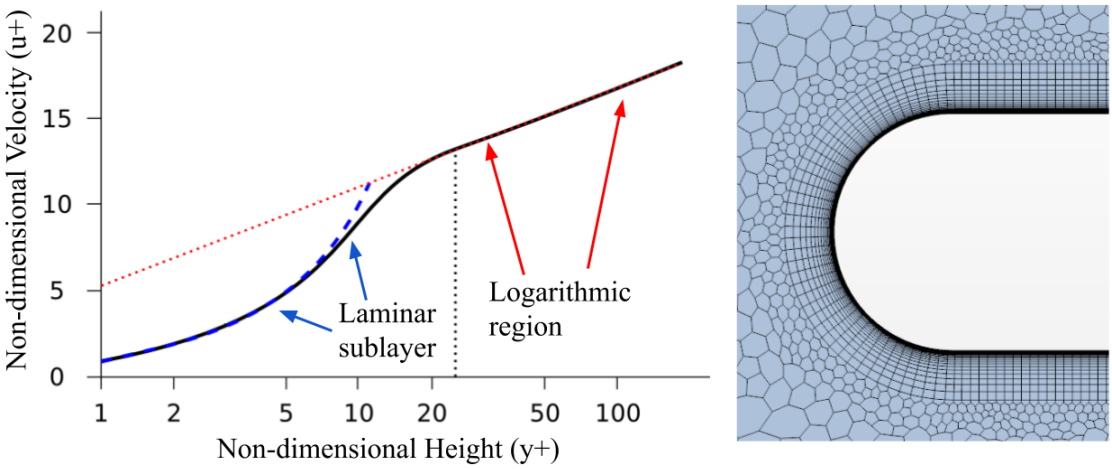

Figure 1.7: Non-dimensional law of the wall boundary layer profile [11] and prism layer cells over a bluff body.

The size of the first prism layer height can be estimated in order to meet a $y+$ value of 1 at the wall from the following calculations. In a turbulent boundary layer over a flat plate, the non-dimensional shear stress, or skin friction coefficient (C_f), can be modeled as a function of the local Reynolds number (Re_x) over the flat plate in Equation 1.9 below.

$$C_f = \frac{0.058}{Re_x^{\frac{1}{5}}} \tag{1.9}$$

The dimensional shear stress (τ_{wall}) can then be calculated based on the skin friction coefficient (C_f), freestream density (ρ_∞) and velocity (u_∞) in Equation 1.10.

$$\tau_{wall} = \frac{C_f \rho_\infty u_\infty^2}{2} \tag{1.10}$$

The shear stress can then be expressed in units of velocity called the shear velocity (u_{fric}) in Equation 1.11 below, using the dimensional shear stress (τ_{wall}) and freestream density (ρ_∞).

$$u_{fric} = \sqrt{\frac{\tau_{wall}}{\rho_\infty}} \tag{1.11}$$

Finally, the required physical prism layer height at the wall (y) can be calculated based on freestream viscosity (μ_∞) and desired $y+$ divided by the shear velocity (u_{fric}) and freestream density (ρ_∞), shown in Equation 1.12.

$$y = \frac{\mu_\infty y+}{u_{fric}\rho_\infty} \tag{1.12}$$

1.4 Ideal Gas Model in STAR-CCM+

A relation for the gas properties in the Navier Stokes equations must be formed through a gas model. Density is nearly constant in very low speed flows when the Mach number is generally lower than 0.3. A higher Mach number results in the density of the air changing when coming in contact with an object and moving around it. This can be modeled at different levels of complexity. A common lower-order yet powerful form of modeling a gas for compressible flows is the ideal gas law, which is the gas model used in STAR-CCM+ for this thesis. The governing equation for an ideal gas is shown in Equation 1.13 below, which proportionally relates the pressure of a gas (p) to its density (ρ) and temperature (T) by a constant (R).

$$p = \rho RT \tag{1.13}$$

The relationship between the isobaric specific heat of air (c_p) and the isochoric specific heat of air (c_v) is constant for an ideal gas when the gas temperature is generally

near standard conditions. This ratio is referred to as the ratio of specific heats (γ) in equation 1.14.

$$\gamma = \frac{c_p}{c_v} \tag{1.14}$$

At higher gas temperatures the ratio of specific heats is no longer constant. One method of modeling this with the ideal gas model is to assume that the isobaric specific heat (c_p) is a polynomial function of temperature (T). This polynomial can be utilized in STAR-CCM+ for the ideal gas model. The coefficients and order of the polynomial are specified for specific temperature ranges. Equation 1.15 is the 5th order polynomial used in this thesis with the coefficients (a_0 through a_5) used across the two temperature ranges starting from the minimum temperature (T_{min}) and maximum temperature (T_{max}) in Table 1.1, which were selected based on the maximum stagnation temperature of the wind tunnel tests replicated in CFD for this thesis. The coefficient values were obtained from previous hypersonic simulation work done in STAR-CCM+ performed by Cross and West [12], which is further discussed in Chapter 2.

$$c_p = a_0 + a_1 T + a_2 T^2 + a_3 T^3 + a_4 T^4 + a_5 T^5 \tag{1.15}$$

Table 1.1: Isobaric specific heat polynomial coefficients from previous hypersonic simulation work done in STAR-CCM+ [12].

	Range 1	**Range 2**
T_{min}	0° K	200° K
T_{max}	200° K	1000° K
a_0	1.003×10^{3}	1.000×10^{3}
a_1	—	9.486×10^{-2}
a_2	—	-8.455×10^{-4}
a_3	—	2.633×10^{-6}
a_4	—	-2.608×10^{-9}
a_5	—	8.668×10^{-13}

The two other key properties that can be changed as a function of temperature with the ideal gas model are viscosity (μ) and thermal conductivity (k), both of which see substantial changes at higher temperatures in hypersonics. A well-defined method for defining these properties at varying temperatures is Sutherland's Law. This method is also utilized in STAR-CCM+ for the ideal gas model and is also recommended for use from previous hypersonic work done by Cross and West [12]. Equation 1.16 and 1.17 are both Sutherland's Law for modeling viscosity and thermal conductivity, respectively, with the gas temperature (T), reference value (k_{ref} and μ_{ref}), reference temperature (T_{ref}), and Sutherland temperature (S).

$$\mu = \mu_{ref} \left(\frac{T}{T_{ref}} \right)^{\frac{3}{2}} \frac{T_{ref} + S}{T + S} \tag{1.16}$$

$$\mu_{ref} = 1.716 \times 10^{-5} Pa \cdot s \qquad S = 111.0°K \qquad T_{ref} = 273.15°K$$

$$k = k_{ref} \left(\frac{T}{T_{ref}} \right)^{\frac{3}{2}} \frac{T_{ref} + S}{T + S} \tag{1.17}$$

$$k_{ref} = 0.02414 \frac{W}{m} \qquad S = 194.0°K \qquad T_{ref} = 273.15°K$$

Chapter 2

MOTIVATION

Chapter 2 goes over the publicly available work that covers CFD simulations of hypersonic flow fields in STAR-CCM+ and how they were utilized to form the objective of this thesis. There are plenty of publicly available subsonic CFD studies in STAR-CCM+ but there are very few that focus on hypersonics. This is most likely due to the fact that a lot of recent research in hypersonics is classified information that surrounds the subject matter of hypersonic weapons, such as nuclear warheads and cruise missiles. Four different older works that are publicly available are discussed in Section 2.1. For each work, the specific hypersonic scenarios were examined along with the best practices used for simulating them in CFD. Not all of the existing work was run in STAR-CCM+, but the practices are of interest. Only certain best practices were selected for running the CFD simulations in this thesis, which helped form the thesis objective stated in Section 2.2.

2.1 Existing Work

Shellabarger [13] analyzed 2D flat plate simulations in STAR-CCM+ at Mach 11 in laminar flow with a ramp at the end of the flat plate. Laminar flow was assumed due the low Reynolds number of 3×10^4. An ideal gas model was utilized but the ratio of specific heats was assumed to be constant throughout the entire flowfield. The goal of the study was to predict the upstream influence as the angle of the ramp would increase. Figure 2.1 is a rendered numerical Schlieren view of one of the angled ramps behind the plate. Flow separation was observed near the junction where the flat plate and ramp were joined, which was determined based on the observed reduction in the local wall shear stress even though

there was no comparison of simulation predictions to experimental data. The theoretical trends were predicted without confirming the accuracy or precision of the simulation with experiments, so there were no best practices to be utilized from this study.

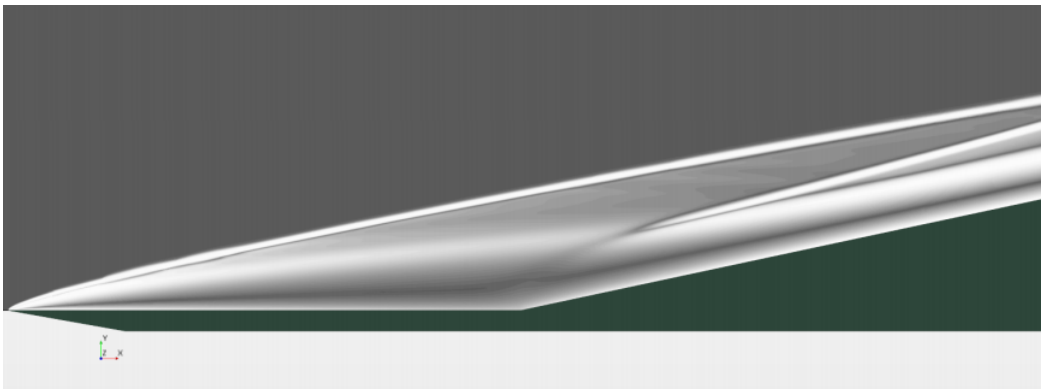

Figure 2.1: Numerical Schlieren of flat plate with downstream ramp at Mach 11 [13].

Wood [14] analyzed a 2D flat plate in hypersonic flow at Mach 6 in Ansys Fluent. While the study was not done in STAR-CCM+, the analysis was useful with regards to it's meshing practices utilized for hypersonic CFD simulations and it's comparison to experimental data. A transition model was utilized with a particular turbulence model that works well with hypersonic cases (k-ω SST model), so the transition from laminar to turbulent flow in the boundary layer on the flat plate was predicted. Because the flow was not entirely laminar, the prism layer cells were sized with a target $y+$ of 0.1 and a growth rate of 1.2 to account for the areas of turbulent flow on the flat plate surface. The boundary layer (BL) height from the wall (δ) from the simulation results was shown to have matched the overall trend when compared to experimental data. The boundary layer height is plotted against non-dimensional location in Figure 2.2 with CFD results (x symbols), experimental data (blue line) compared to the theoretical curves (dashed and solid black lines). While the comparison was primarily qualitative by comparing the height profiles, the $y+$ target and growth rate values were adopted for usage in the CFD simulations of this thesis, given that they were utilized for achieving some form of validation for a hypersonic boundary layer.

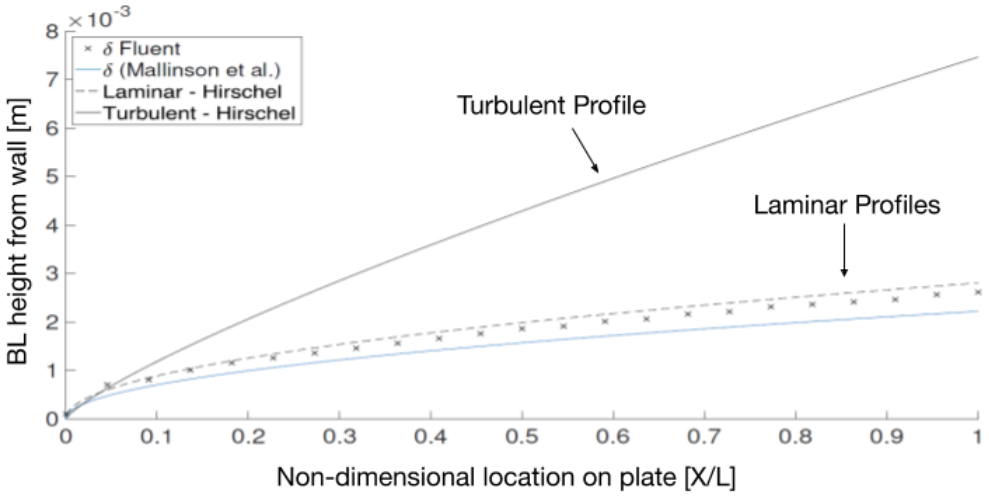

Figure 2.2: CFD boundary layer height compared with experimental height data and theoretical heights [14].

Richardson [15] ran 3D simulations in STAR-CCM+ that replicated overall aerodynamic force loads of a 70° swept delta wing wind tunnel model at Mach 6.8 and 9.6. The wind tunnel data was from NASA Report R-153, which compared the measured aerodynamic loads and surface pressure coefficient distributions from wind tunnel tests to predicted loads from analytical data. The CFD simulations assumed an ideal gas with isobaric specific heat capacity of air as a polynomial function of temperature. It is not stated if the STAR-CCM+ default polynomial values were used or if they were modified to more accurately represent the ratio of specific heats for air, like the coefficients utilized by Cross and West [12]. Fully turbulent flow was assumed by using the k-ω SST turbulence model. To refine the mesh around the surrounding shocks automatically, an adaptive mesh refinement technique was implemented in STAR-CCM+ to refine the mesh where a strong gradient in Mach number was detected. Figure 2.3 below shows the shape of the delta wing and the automatically refined mesh around it. The aerodynamic loads and pressure coefficient distributions showed good qualitative and quantitative agreement with CFD results at lower angles of attack. Quantitative error was not specified however. Because the study did not analyze heat transfer loads or compare the simulation results to studies that did not

use the adaptive mesh refinement technique, this did not provide justification for utilizing adaptive mesh refinement for the scope of this thesis.

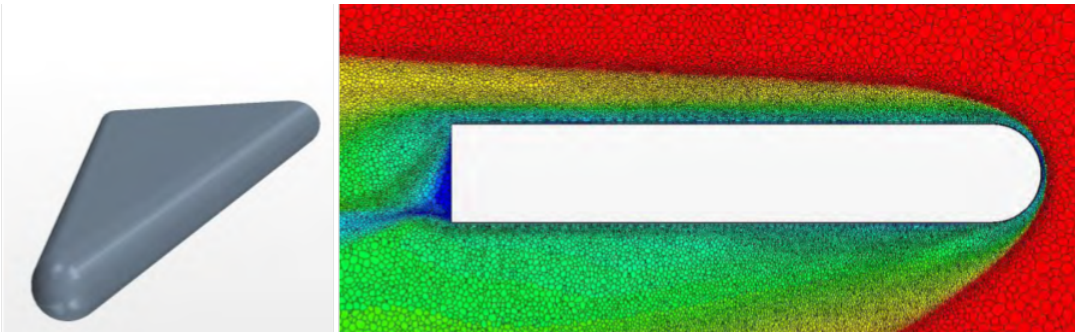

Figure 2.3: 70° swept delta wing with adaptive mesh refinement around surrounding shockwaves [15].

Cross and West [12] ran a very wide range of hypersonic CFD simulations in STAR-CCM+ for predicting primarily heat transfer loads. There was also a focus on determining what best practices should be utilized for hypersonic simulations in STAR-CCM+. The geometries of interest were primarily double cones, hollow forward-facing cylinders with a flare, and cylinders in crossflow with an impinging shock. The Mach number ranged from 5.9 to 13.2 in both laminar and turbulent flow. Turbulent flow was modeled with the k-ω SST model and Spalart Allmaras model. The target wall $y+$ when using the turbulence models was kept under 1. The regions of separated flow were of interest with regards to heat transfer loads in the CFD simulations. Their cases that assumed laminar flow or turbulent flow with the Spalart Allmaras turbulence model would underpredict the heat transfer loads, but turbulent cases with the k-ω SST model would overpredict the heat transfer loads. It is not mentioned what the relative error was of these loads when compared to wind tunnel data.

Cross and West [12] also used a multi-species gas model, which is a complex gas model for air that includes chemical reactions at high temperatures. For a single species model, the ratio of specific heats was assumed to be a polynomial function of temperature up to 6000° K. The coefficients for a temperature range of 0° K to 1000° K are utilized

for this thesis, as listed in Table 1.1 from Chapter 1. Like the work done from Richardson [15], an adaptive mesh refinement technique was used to refine the mesh automatically around shockwaves based on pressure gradient. Because of the 2D nature of the experimental data, which was mostly axisymmetric cones and cylinders, all CFD simulations run by Cross and West [12] were done in 2D. This allowed the utilization of meshes that had high levels of refinement around the shocks, resulting in mesh cell count that was on the order of half a million cells in some simulations. The level of detail required in the simulations necessitated the use of the adaptive mesh refinement, but it was primarily for regions with separated flow and shocks. Figure 2.4 shows the wind tunnel model for the double cone configuration and a mesh with adaptive mesh refinement for an impinging shock on a cylinder in cross flow. Since these flow features were not of interest in this thesis, the adaptive mesh refinement method was not used.

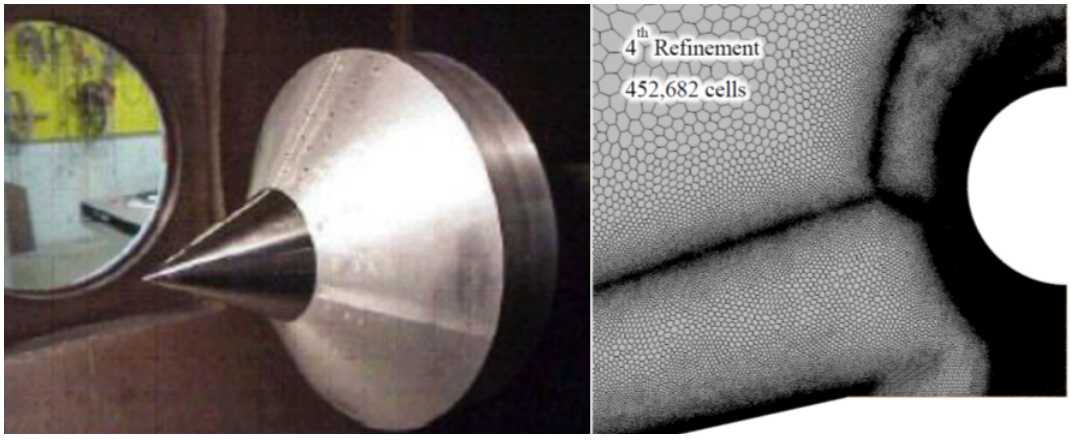

Figure 2.4: Wind tunnel double cone model and adaptive mesh refinement for an impinging shock on a cylinder in cross flow [12].

2.2 Objective

The previous work provided a wide range of insight on what analysis has already been done in hypersonic STAR-CCM+ simulations and what best practices should be used. It was observed that there hasn't been any previous work done on predicting localized heat

transfer loads on the most forward-facing surfaces, such as the leading edges of bluff bodies in hypersonic flow. Most of the previous work focused on loads that appear downstream in other regions of interest, but best practices from previous work were taken into account. The objective of my thesis is to characterize and quantify the capabilities of STAR-CCM+ in predicting the peak heat-transfer loads on the leading edge of a swept delta wing re-entry body in laminar flow with an ideal gas model without adaptive mesh refinement.

Chapter 3

VALIDATION CASE

Chapter 3 covers a hemisphere-cylinder validation case that was run prior to running the primary delta wing simulations in Chapter 4. This validation case served as a simpler and less computationally-expensive simulation to help with the selection of STAR-CCM+ physics settings and meshing practices for the delta wing simulations. The meshing practices were set up with a methodology that could also be applied to the delta wings despite being on a different scale. Section 3.1 goes over the background of the original hemisphere-cylinder wind tunnel study that this validation case was based on. Section 3.2 covers the selection of STAR-CCM+ CFD solver and mesh settings. Section 3.3 shows the results of the mesh convergence study, while Section 3.4 provides an overview of the STAR-CCM+ results in comparison with hemisphere-cylinder wind tunnel data.

3.1 Validation Case Background

The geometry of the validation case is a hemisphere-cylinder, which is a cylinder that's facing forward into the freestream with a hemisphere on the forward end. A forward-facing hemisphere is a fundamental shape in hypersonics, being a simple bluff body shape with easily defined geometry to test and measure hypersonic loads on. The specific case for validation was replicated in CFD from NACA Technical Report 1323, which tested a hemisphere-cylinder near Mach 6.8 in the Langley 11-inch hypersonic wind tunnel. The model had a diameter of 3.025 in and an overall length of 10.5 in. Heat transfer loads were obtained by measuring the change in individual thermocouple temperature measurements over time to calculate heat transfer coefficients, which were used to calculate the Nusselt

number. The Nusselt number was then divided by the square root of the Reynolds number. It was not stated why this was done in the original report but it was presumably for scalability reasons to rule out dependency of Reynolds number. This non-dimensional heat transfer load was referred to as a heat transfer parameter in the original report [16], but for clarity purposes it is referred to as scaled Nusselt number in this thesis to differentiate from other heat transfer parameters that are mentioned. Freestream conditions behind a normal shock were used as reference values for the Nusselt number and Reynolds number when calculating scaled Nusselt number [16].

Calculations to take into account the loss of heat from the wind tunnel model through radiation were not performed in the report, but associated error was estimated to be about 3% at the stagnation point where gas temperature was the highest. Error due to variation in wall temperature at the stagnation point was estimated to be 1.5% [16].

The measurements of heat transfer were taken along the 2D profile of the geometry. This consisted of a quarter of a circular arc on the hemisphere face and a straight line on the cylinder surface downstream. This profile is referred to as the non-dimensional surface path in this thesis, and is symbolized with x/b from the original report with x being the dimensional generatrix path and b representing a quarter of the hemisphere's circumference. The original model had the thermocouples arranged in a spiral fashion around the hemisphere and cylinder to space them out as far as possible. This however did not change the position of the thermocouples along the axis of the model, which meant that the path of the measurements could still be interpreted as a 2D non-dimensional surface path. This non-dimensional surface path (x/b), which is based on the model generatrix, is visually illustrated in Figure 3.1. Dimensions of the hemisphere-cylinder are labeled above a photograph of the original wind tunnel model.

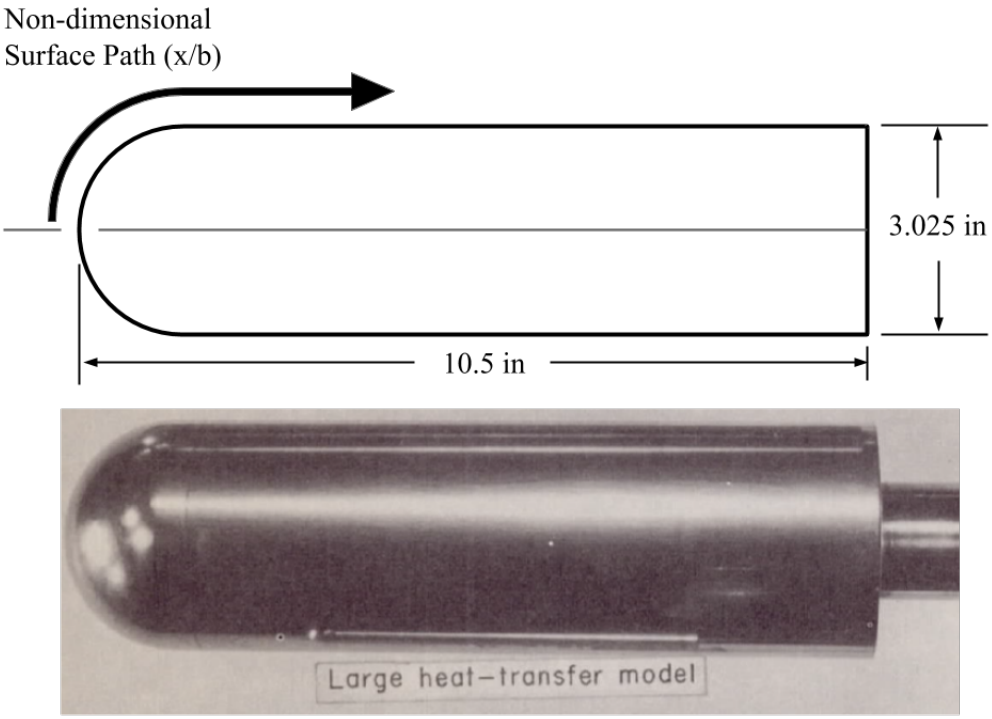

Figure 3.1: Non-dimensional surface path with dimensions and original wind tunnel model [16].

The hemisphere-cylinder was tested across a wide range of Reynolds numbers, ranging from 0.14×10^6 to 1.06×10^6 with respect to diameter. The adjustments in the freestream conditions to change the Reynolds number resulted in the Mach number ranging from 6.74 to 6.82 for the tests, with the stagnation temperatures ranging from about 1040°R to 1160°R [16]. Only one of the tests however had an initial surface temperature provided, which is necessary for replicating heat transfer loads in CFD. The freestream conditions for this specific test are provided in Table 3.1. The reference conditions past a normal shock based on the Mach number are in Table 3.2 and denoted by subscript σ for calculating scaled Nusselt number. Unfortunately the only provided freestream conditions in the original report for the specific test were Reynolds number based on freestream conditions and Reynolds number based on conditions behind a normal shock. In order to be sure that the freestream conditions from the study were consistent with CFD, the freestream con-

ditions were calculated based on the freestream Reynolds number. The resulting Reynolds number based on normal shock conditions was calculated and it was shown that it did not exactly match the published value. As seen in Table 3.2, the calculated Reynolds number does not exactly match what was specified from the test, but it was the closest that could be obtained from the range of freestream conditions that were provided. This combination of freestream conditions ended up utilizing the lowest Mach number and highest stagnation temperature from the report to best match the Reynolds number. Isentropic relations for compressible flow were utilized for calculating the freestream conditions based on the Mach number and stagnation conditions. Sutherland's law was utilized for determining the reference viscosity and reference thermal conductivity from equations 1.16 and 1.17 respectively. Published values from the original report are denoted with an asterisk.

Table 3.1: Validation case freestream conditions [16].

Mach Number (M_∞)	6.74*
Stagnation Pressure (p_o)	1.17 MPa
Stagnation Temperature (T_o)	644°K (1160° R)*
Static Pressure (p_∞)	351 Pa
Static Temperature (T_∞)	63.9°K
Viscosity (μ_∞)	4.30×10^{-6} Pa-s
Reynolds Number (Re_D)	3.7×10^5*
Initial Model Temperature (T_i)	325°K (125° F)*

*original published value

Table 3.2: Reference conditions past a normal shock [16].

Mach Number (M_σ)	0.40
Static Presssure (p_σ)	18.5 kPa
Static Temperature (T_σ)	625°K
Thermal Conductivity (k_σ)	0.0477 W/m-K
Viscosity (μ_σ)	3.10×10^{-5} Pa-s
Reynolds Number (Re_σ)	0.51×10^5 (0.52×10^5)*

*original published value

3.2 Validation Case Methodology

The governing STAR-CCM+ physics and solver settings used for the validation case are shown in Table 3.3 with explanations next to each one.

Table 3.3: Solver settings used for validation case.

Setting	Selected Option	Comments
Flow Solver Approach	Coupled Flow	Solves Navier Stokes equations together as coupled equations, preferable for hypersonics.
Time Dependency	Steady	Leading edge flow in hypersonics is predominantly steady.
Gas Model	Ideal Gas (Equation 1.13)	Single species gas that obeys the ideal gas law.
Viscosity	Sutherland's Law (equation 1.16)	Function of temperature only.
Isobaric Specific Heat	Polynomial in T (equation 1.15)	Function of temperature only. Polynomial coefficients from Cross and West [12].
Thermal Conductivity	Sutherland's Law (equation 1.17)	Function of temperature only.
CFL Control	Automatic selection from 0.1 to 1.0	CFL kept at or below 1.0 to keep simulation stable.
Continuity Convergence Accelerator	Enabled with default settings.	Convergence accelerator, minimizes mass residual across each cell.
Viscous Regime	Laminar	Laminar flow is assumed everywhere in the flowfield.
Turbulence Model	k-ω SST	Turbulent flow is assumed everywhere in the flow field, used for only one turbulent CFD simulation to check $y+$.

An axisymmetric 2D domain and a 3D domain with a symmetry plane were both used for the validation case to check for any discrepancies that may have appeared between 2D and 3D simulations with regards to meshing and simulation results. The primary delta

wing cases in Chapter 4 are 3D with one symmetry plane, so any practices learned with a symmetric 3D domain could be potentially utilized in the delta wing cases.

There was also no need to have a large domain surrounding the model since the simulation was hypersonic, so long as shocks were not reflected off the surrounding domain surfaces. It was also sized such that the prism layers on the hemisphere-cylinder body would not be affected by any proximity mesh refinement due to being too close to the farfield walls. The driving domain dimensions are shown below in Figure 3.2, expressed in terms of diameter, with an angled view of the complete domain. Only the driving dimensions are shown since the diameter and length of the hemisphere-cylinder are already known. The blue wall on the left of the completed domain is the symmetry plane and the transparent tan surfaces represent the farfield boundary condition.

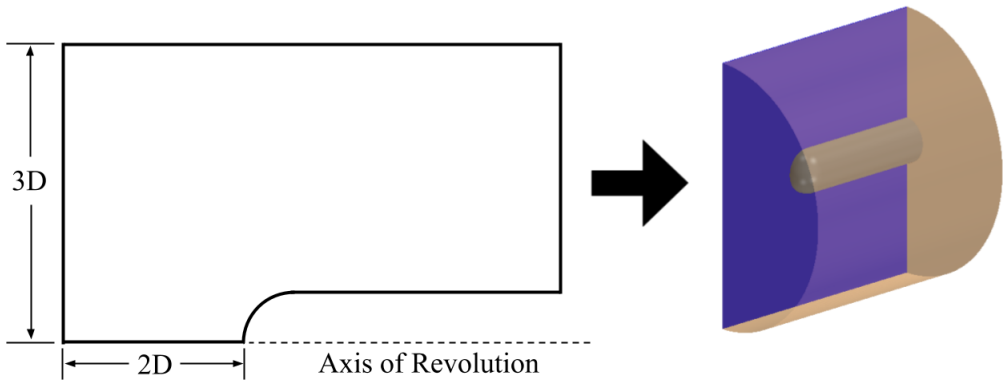

Figure 3.2: 2D domain profile with dimensions and resulting cylindrical domain.

Because the case was run with viscous flow, prism layer cells had to be utilized to capture viscous effects. The first prism layer cell height was calculated using equations 1.9 through 1.12 assuming a $y+$ of 0.1 assuming turbulent flow. Reference length was chosen to be the total non-dimensional surface path x/b along the length of the model but dimensionalized by multiplying it by b. The prism layers were grown outward until an aspect ratio near 1 was achieved, which is the ratio of a cell's height to its overall width. This was done to make the final prism layer cells have a near-uniform shape before transitioning to the non-prism layers cells that grow away from the surface of the geometry.

A growth rate of 1.2 was selected for prism layer growth rate. STAR-CCM+ only allows input of total prism layer count and total prism layer thickness when the first layer height is specified. The total prism layer count and thickness were calculated based on the growth rate and initial prism layer height. The final prism layer height was determined when an aspect ratio of 1 was reached. A 2D visual representation of how this calculation was done is represented in Figure 3.3 with a visual example in STAR-CCM+.

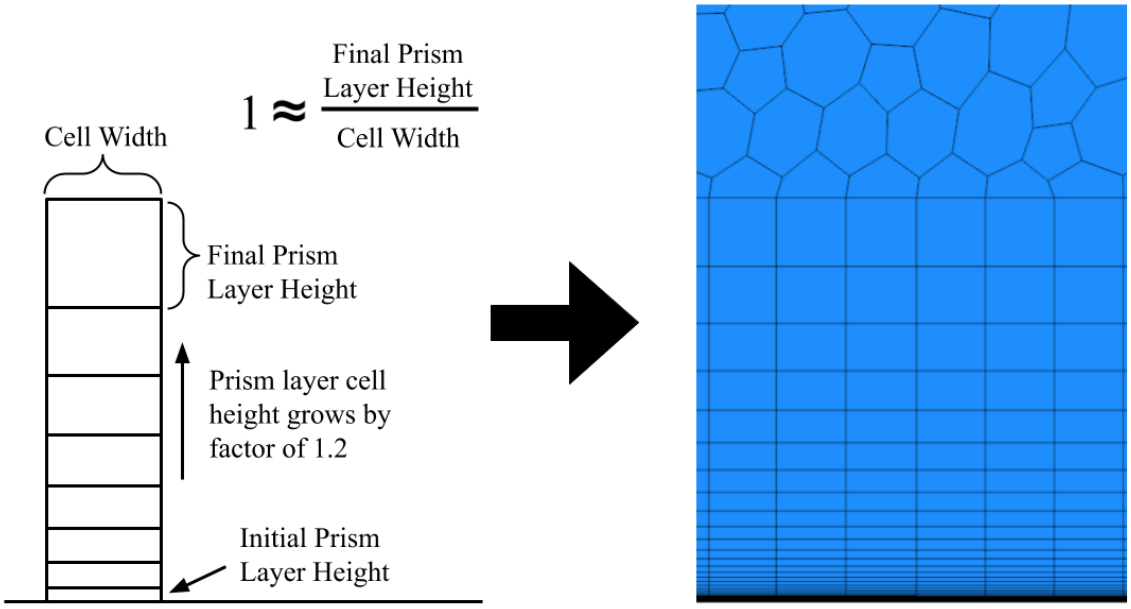

Figure 3.3: 2D graphic of prism layer growth and an actual prism layer mesh in STAR-CCM+.

The prism layers controlled the refinement of the mesh in the direction normal to the surface, but refinement in the circumferential direction around the hemisphere was handled differently. One way that the STAR-CCM+ handles the refinement around curvature is ensuring that there is a minimum number of points per circle. The default value is 36 points per circle, which means that in a cross section of a spherical or cylindrical surface there are 36 vertices total, which results in a cell size that's about 8.7% of the diameter of the circle. This points per circle concept is visually demonstrated in a 2D fashion in Figure 3.4 with the front of the hemisphere-cylinder having a coarse mesh refinement of 30 points per circle.

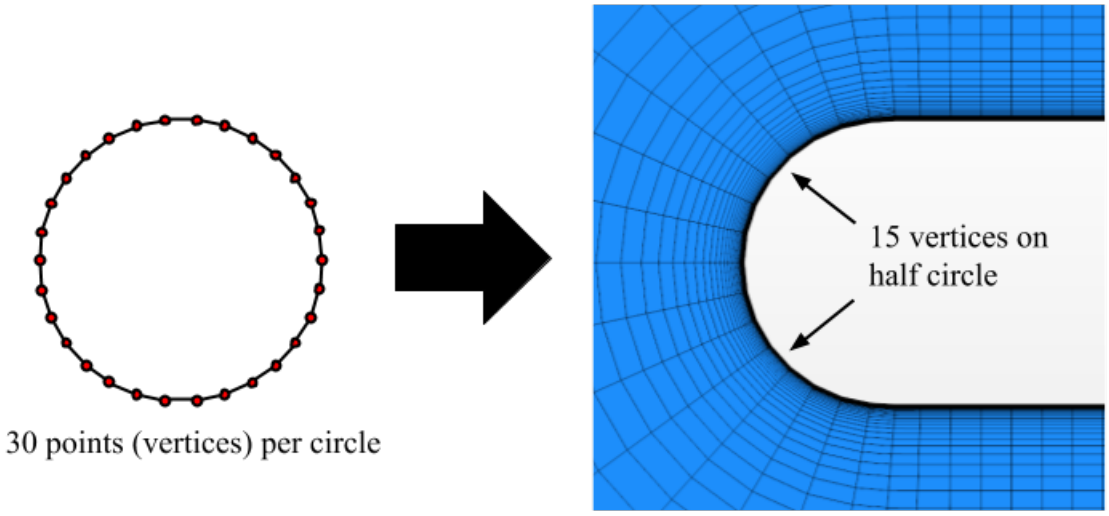

Figure 3.4: Visual representation of using points per circle for refining circular surfaces.

This technique of controlling the prism layer cells and the refinement in the circumferential direction was used for the mesh convergence study in the next section. The other primary STAR-CCM+ mesh settings that were utilized are listed in Table 3.4 with regards to the farfield target cell size to ensure the cells grew at the growth rates specified.

Table 3.4: Other required mesh settings utilized in STAR-CCM+ for validation case.

Base Size	3.025 in (1 diameter)
Target Cell Size	1000% of base size
Surface Growth Rate	1.1
Volume Growth Rate	1.1

3.3 Validation Case Mesh Convergence Study

A mesh convergence study was performed for the 3D domain to determine the appropriate level of mesh refinement needed to capture the heat transfer loads. This was done by reducing the minimum cell size on the geometry as a function of percentage of diameter. The first mesh level used a minimum cell size of 8.7%, which equates to the default 36 points per circle setting in STAR-CCM+ described in Section 3.2 previously. Because of

the reduced cell size in the circumferential direction, the calculations for determining the number of prism layers and the total prism layer thickness had to be redone for each new cell size in order for the final prism layer to have an aspect ratio near 1. These values are listed in Table 3.5 below, with the first prism layer cell height being 5.02×10^{-7} m.

Table 3.5: Mesh levels used for mesh convergence study.

Mesh level	1	2	3	4
Minimum Cell Size	8.7%*	7%	5%	3%
Prism Layer Count	53	51	50	47
Total Prism Layer Thickness	4.7 cm	3.3 cm	2.7 cm	1.6 cm
Domain Cell Count	34,959	42,935	58,211	106,393

*default 36 points/circle value in STAR-CCM+

The mesh convergence study was performed by looking at the relative change in net drag, net heat transfer, and scaled Nusselt number at the stagnation point from the previous mesh level. The relative change for the net drag and heat transfer was within $\pm 2\%$ across all four mesh levels. The maximum relative change for scaled Nusselt Number was -2.9% from mesh level 2 to 3, but closer inspection showed that the final value at mesh level 4 was within -2% of the original value at level 1. The other loads at mesh level 4 were within $\pm 2\%$ of the loads at mesh level 1. Because of the load similarity between the coarsest mesh level and the finest mesh level, mesh level 1 was utilized for this validation case study. The relative change between the four mesh levels is plotted in Figure 3.5 against cell count at the next mesh level, which in this case corresponds to cell count for level 2, 3 and 4 from left to right. Table 3.6 contains the load values across the four mesh levels and the relative change from the previous mesh level.

Settings from mesh level 4 of the convergence study for the 3D case were used for the 2D case. This was because the 2D case failed to converge with the settings from the coarser mesh levels. The 2D case also failed to converge with settings that produced a mesh that was more refined than mesh level 4.

Table 3.6: Load values at each mesh level.

Mesh Level	1	2	3	4
Domain Cell Count	34,959	42,935	58,211	106,393
Net Drag	23.03 N	23.15 N (0.5%)*	23.19 N (0.2%)*	23.43 N (1.0%)*
Net Heat Transfer	209.1 W	206.4 W (-1.3%)*	205.1 W (-0.6%)*	204.9 W (-0.1%)*
Scaled Nusselt Number at Stagnation Point	1.948	1.962 (0.7%)*	1.906 (-2.9%)*	1.935 (1.5%)*

*Relative change from previous mesh level

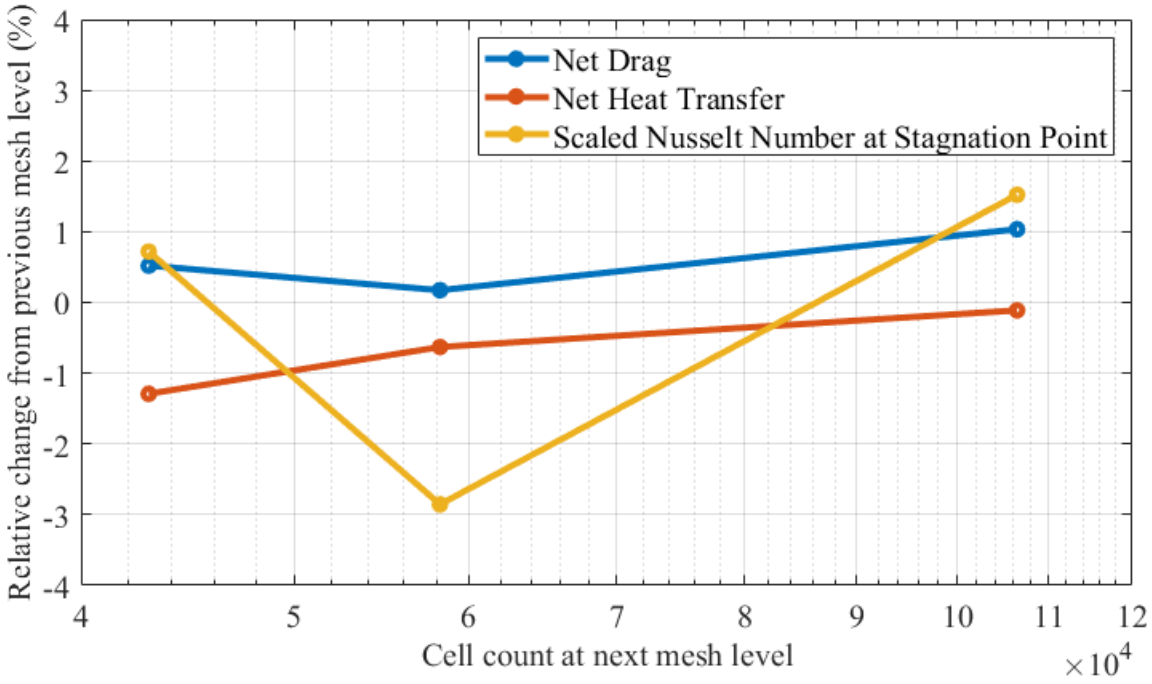

Figure 3.5: Relative change between each of the four mesh levels studied against cell count of the next mesh level.

A contour scene based on Mach number was generated on the symmetry plane of the 3D case and on the full domain for the 2D case to verify that the farfield walls were clear of any shocks at the selected mesh levels. It was shown that no shocks were in contact with the farfield walls. Figure 3.6 shows the contour scene with Mach number for the 3D case and Figure 3.7 shows the contour scene with Mach number for the 2D case.

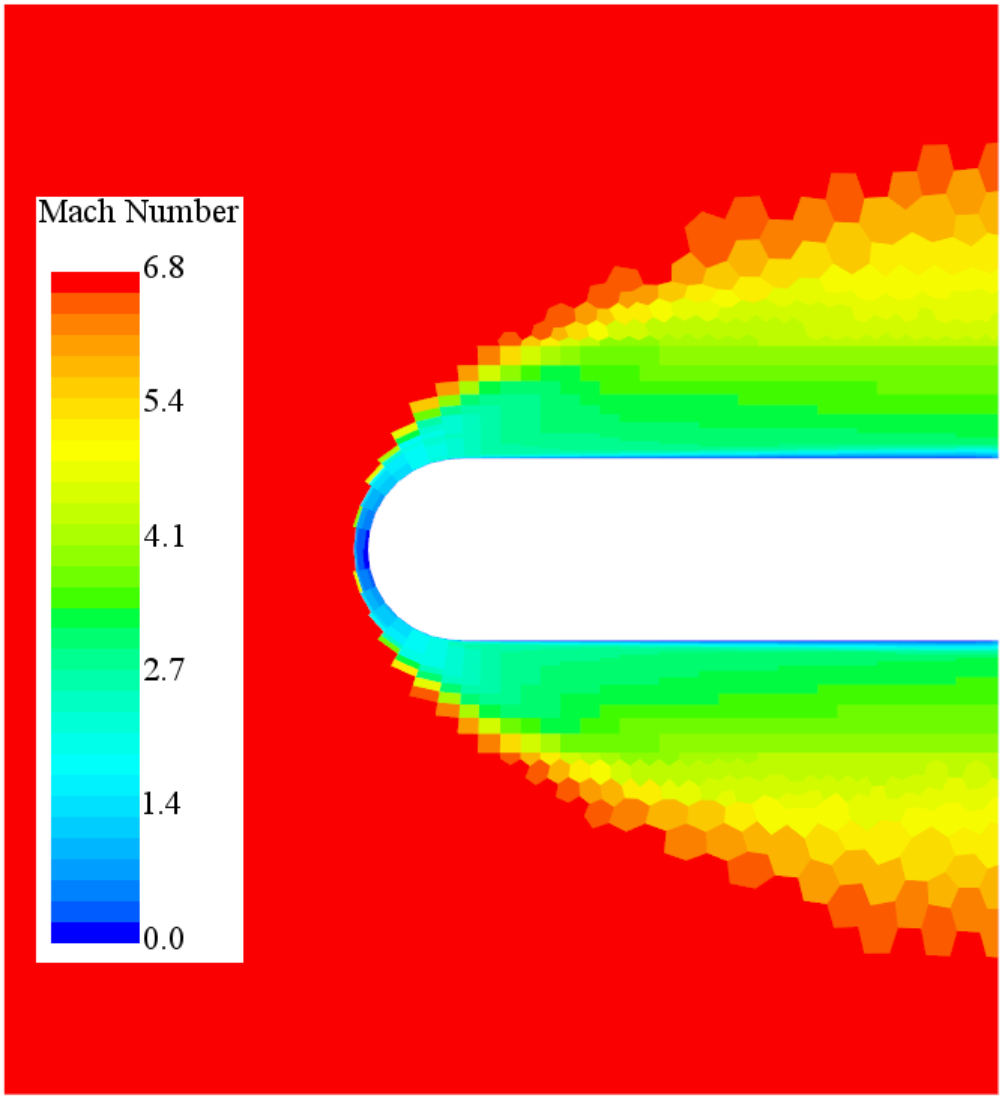

Figure 3.6: Contour scene of Mach number in the symmetry plane of the 3D case showing no shocks hitting the boundaries of the farfield.

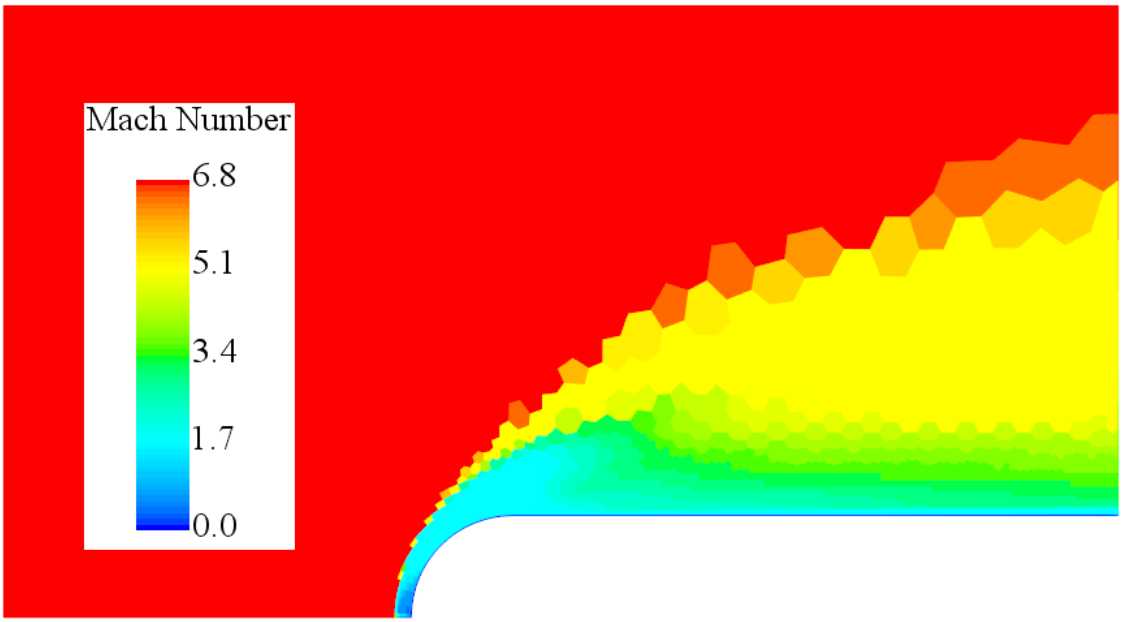

Figure 3.7: Contour scene of Mach number for the 2D case showing no shocks hitting the boundaries of the farfield.

To verify that the prism layers had sufficient resolution near the wall, the selected level of mesh refinement was run in a 3D fully turbulent flow case to check that the wall $y+$ was on the order of 0.1. It was shown that a majority of the wall y+ was near or under 0.1 except for some cells that surrounded the stagnation point where the highest $y+$ was 0.18. The case was run again with a first prism layer height that was an order of magnitude smaller but this did not reduce $y+$. The smaller prism layer height was 5.02×10^{-8} with a total of 65 prism layer cells used and a total prism layer height of 4.7 cm. The contour scene of the hemisphere-cylinder used for checking the y+ is shown in Figure 3.8.

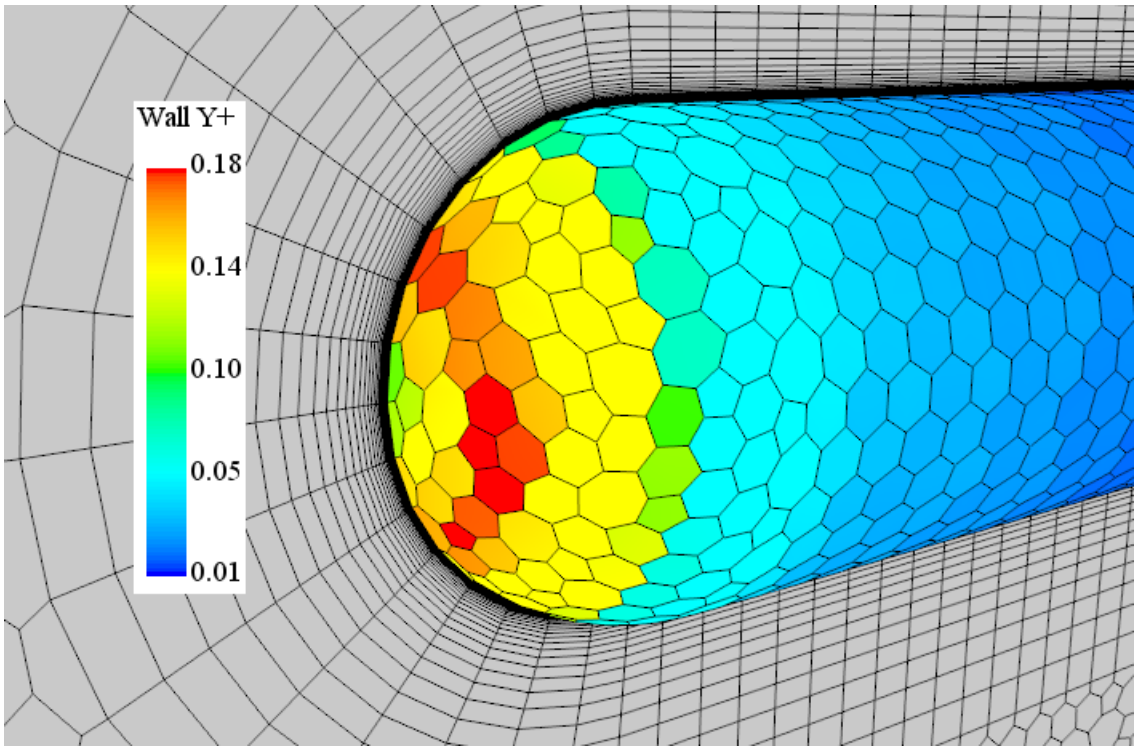

Figure 3.8: Wall $y+$ for turbulent case.

3.4 Validation Case Results

To compare the heat transfer loads between the wind tunnel data and CFD data, the scaled Nusselt number from each cell was first plotted against its corresponding x-coordinate along the x-axis in STAR-CCM+. This was then exported as scaled Nusselt number against x-coordinate data. The x-coordinates were non-dimensionalized by dividing them by the quarter hemisphere circumference value b. The non-dimensional x-coordinates were then converted into non-dimensional surface path x/b. The scaled Nusselt number was then plotted against x/b to compare directly with plotted wind tunnel data.

The 2D case produced a converged result but failed to resolve the heat transfer load for the two cells that were closest to the stagnation point. The heat transfer load at these two cells was overpredicted by up to 383% relative to the peak heat transfer load from wind tunnel data. However, the heat transfer load just downstream of these two cells was overpredicted by only 36%. From a qualitative standpoint, the CFD results on the rest of the hemisphere face did not agree with the wind tunnel data. However, there was much better agreement on the cylinder surface. The wind tunnel data and CFD results are plotted against non-dimensional surface path in Figure 3.9 for the 2D case. The y axis limits of the plot are set such that the CFD data is visually comparable with the wind tunnel data, which means that the highly overpredicted heat transfer loads at the two cells closest to the stagnation point are not shown.

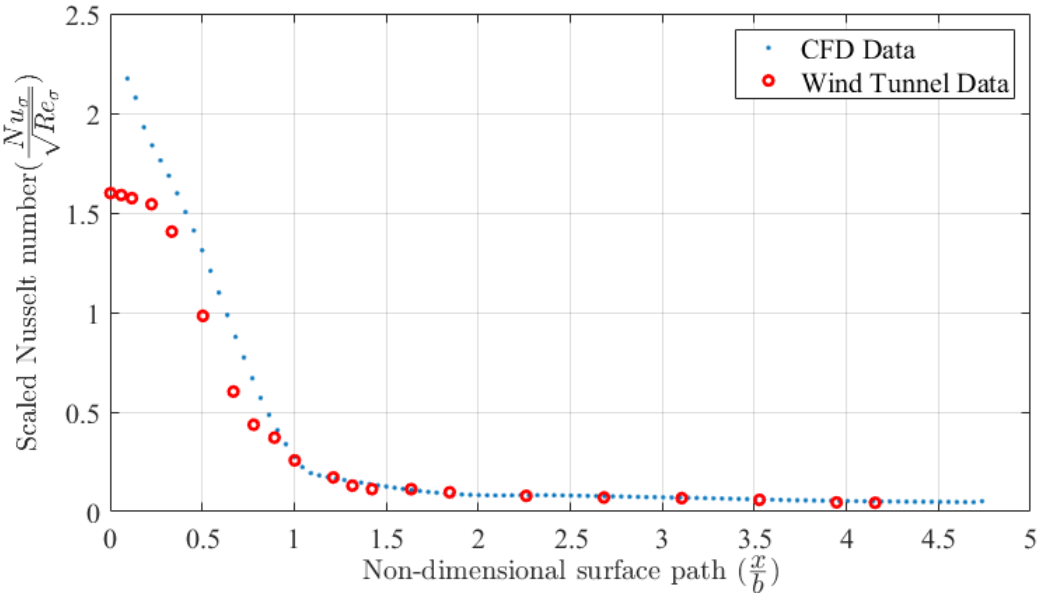

Figure 3.9: Scaled Nusselt number plotted against non-dimensional surface path x/b for the 2D case.

The 3D case produced a much more realistic result when compared to the 2D case. The heat transfer load at the stagnation point was 21.8% higher than that from the wind tunnel data, which is well above the maximum combined wind tunnel data error of 4.5%. This region of overprediction in heat transfer starts near x/b = 0.3, which covers

almost a third of the non-dimensional surface path that lands on the hemisphere face. Qualitatively, the distribution of heat transfer load on the cells near the stagnation point sees a lot more variation in value despite the cells having almost the same x/b location in space. When compared to the area of overprediction in heat transfer near the stagnation point, the CFD agrees much better with wind tunnel data past the x/b location of 0.3 all the way to the end of the hemisphere-cylinder except for the junction between the hemisphere face and cylinder face where x/b = 1. There is also less variation in the heat transfer load at every cell's x/b location. The wind tunnel and CFD results are plotted against non-dimensional surface path in Figure 3.10 for the 3D case.

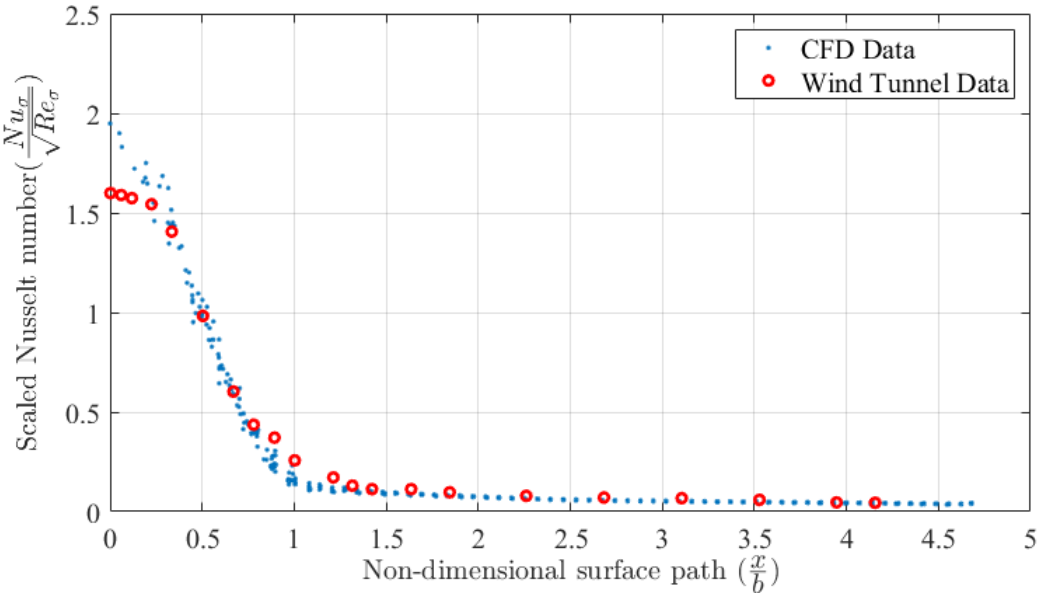

Figure 3.10: Scaled Nusselt number plotted against non-dimensional surface path x/b for the 3D case.

The 3D case was further analyzed because the heat transfer loads near the stagnation point agreed much better with wind tunnel data than the 2D case from both a qualitative and quantitative standpoint. Upon closer examination of the scalar scene cross section, the area near x/b = 0.3 happened to be where the region of subsonic flow began to transition back to supersonic flow. This implied that the subsonic high temperature region was specifically where the overprediction in heat transfer load occured with the physics settings

used. The mesh in this region was very coarse relative to the mesh resolution used by Cross and West [12]. To better resolve this region, a highly refined mesh may be required and entail the utilization of more costly physics settings such as the multi-species gas model that Cross and West [12] used with the adaptive mesh refinement technique, all of which is beyond the scope of this thesis.

The nonuniformity of the heat transfer loads near the stagnation point was most likely due to the nonuniformity of the surface mesh on the hemisphere, given that the uniform heat transfer load distribution past the hemisphere face happened to be where the surface mesh cells were arranged in a uniform pattern on the cylindrical surface. The subsonic region and the scaled Nusselt number distribution across the surface mesh are both shown in Figure 3.11. It is worth noting the differing surface mesh patterns between the hemisphere face, which has non-uniformly arranged surface cells, and cylindrical surface, which has uniformly arranged surface cells.

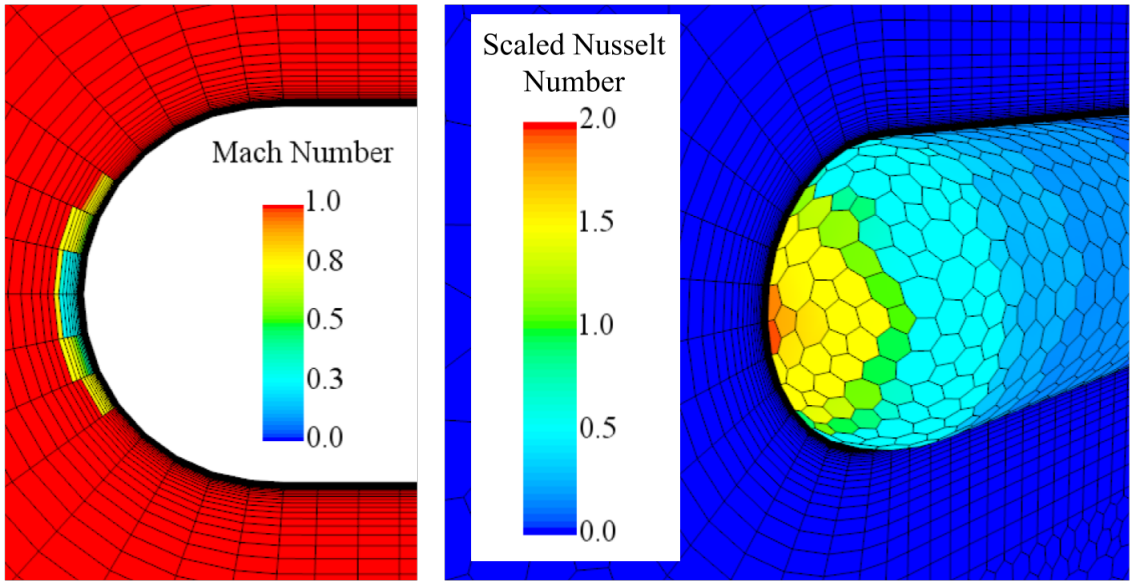

Figure 3.11: Subsonic region and non-uniform mesh distribution.

The lessons learned from this validation case became useful when comparing the results with the delta wing results, which is discussed in Chapter 5. The methodology

for performing the mesh refinement study as well as maintaining the mesh uniformity in the areas of measurement was taken into consideration, which will be explained further in Chapter 4 and 5.

Chapter 4

DELTA WING CASE

This chapter covers the background of the actual NASA report that the delta wing validation data for CFD was taken from. The wind tunnel test that the simulations are based upon is discussed in Section 4.1 along with how it was replicated in CFD in Section 4.2. Section 4.3 covers the results of the mesh convergence study and Section 4.4 contains the simulation results and observations made. Section 4.5 covers the discussion of the delta wing results but the comparison with the validation case is discussed in Chapter 5.

4.1 Delta Wing Background

The source of the hypersonic wind tunnel data for this thesis comes from NASA-CR-535, a NASA technical report that was done to support the X-20 aerothermodynamics. For simplification at the early design stage of the project, the delta wings were defined as triangular planforms with different leading edge curvatures, body lengths, and sweep angles from Mach 2.2 to 15 and Reynolds numbers from 8.38×10^4 to 130×10^4 based on leading edge diameter. Eight different wind tunnel models were tested at six different test facilities to analyze pressure and heat transfer loads. One of the specific quantities of interest was the magnitude of the peak heat transfer load on the delta wing leading edge [6]. A photograph of one of NASA's delta wing models is shown in Figure 4.1.

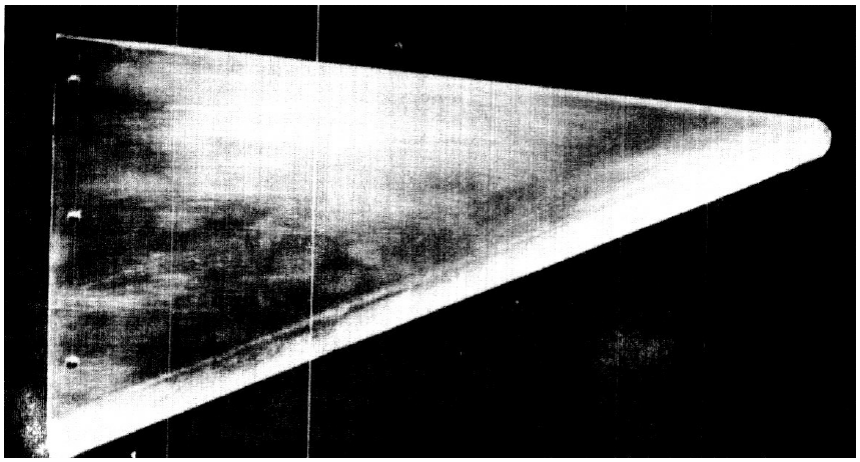

Figure 4.1: Simplified X-20 delta wing wind tunnel model [6].

The heat transfer loads from NASA's wind tunnel test were calculated to determine what the load distribution was on the model during the instant at which the wind tunnel was turned on. This moment in time can be replicated in steady state CFD in STAR-CCM+ as long as the intial temperature of the wind tunnel model is specified as a boundary condition. Since initial model temperature was provided for each test in the original report, the wind tunnel tests were able to be replicated in CFD for this thesis.

Local surface pressures on the leading edge were measured by placing pressure taps on the leading edge of the left-hand side of the delta wing. The final pressure measurements were published as pressure coefficient. Heat transfer loads were measured by placing thermocouples in the same location but mirrored onto the right-hand side of the model and measuring the initial change of surface temperature over time, which was used to calculate the heat transfer coefficients based on initial model temperature. This was then used to calculate the Stanton number. The final heat transfer loads were published as normalized Stanton number, which is the Stanton number divided by a reference Stanton number. The reference Stanton number for each wind tunnel case was based on the theoretical stagnation heat transfer load on a hemisphere that had the same diameter as the delta wing leading

edge in the same freestream conditions[6]. The mirrored placement of pressure tap tubes and thermocouple wires are shown in Figure 4.2 below.

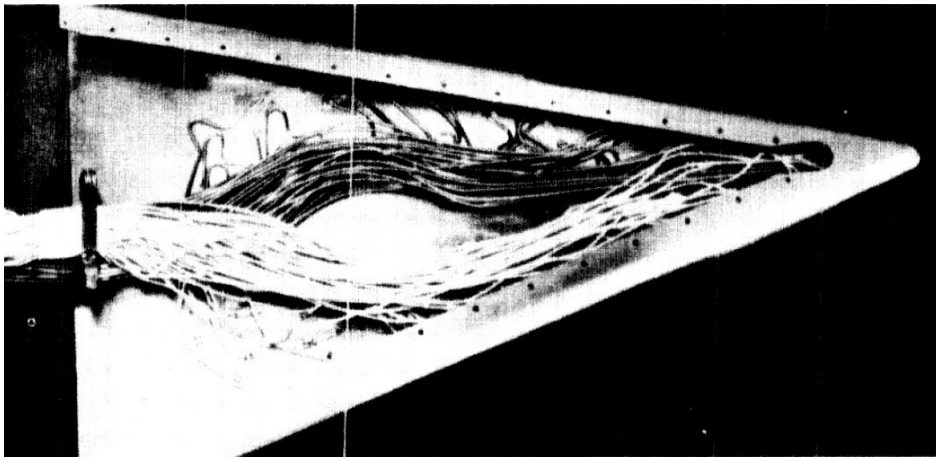

Figure 4.2: Pressure tap tubes (dark) and thermocouple wires (white) installed on opposing sides of the wind tunnel model [6].

Error in the published wind tunnel data was estimated in the original report based on the effects of heat conduction throughout the wind tunnel model and error in the specific heat of wind tunnel model material itself. Both errors were estimated to be 3% [6], resulting in a maximum combined error of about 6%, meaning that if the CFD results agree within 6% of the wind tunnel data, they would be in agreement with each other.

The pressure taps and thermocouples were placed on the model in lines of formation that were normal to the leading edge of the wing. The lines would start at the leading edge and travel along the underside of the wing [6]. This is visually represented in Figure 4.3. In the top-down view of the model, the dashed line representing cross section A-A shows the orientation of the line normal to the leading edge where measurements were taken. The location of the line is defined by non-dimensional centerline location X/D, or the distance between the forward wing tip and where cross section A-A intersects the model centerline divided by the leading edge diameter. In the cross-section A-A, which is to the right of the top-down view in Figure 4.3, the curved path N/D represents the path where measurements were taken along the leading edge surface. It starts at the front of the

leading edge and travels to the underside of the wing. It is non-dimensionalized by dividing it by the leading edge diameter (D).

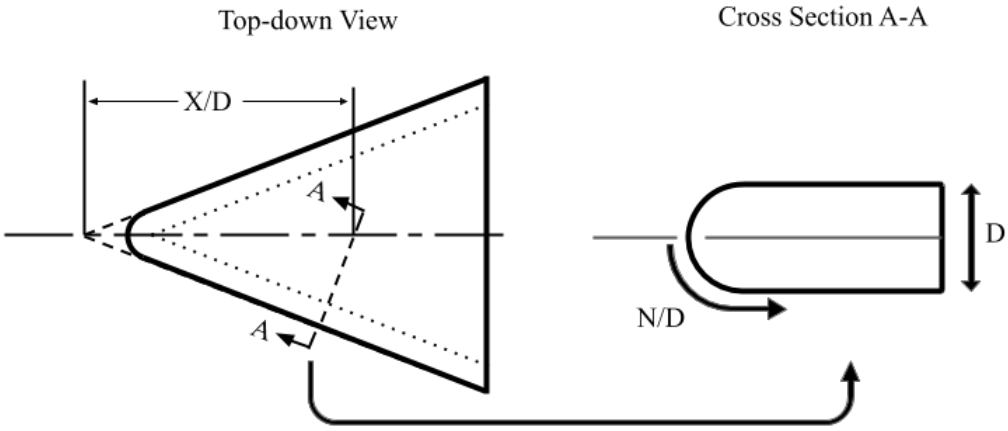

Figure 4.3: Schematic (not to scale) showing location of non-dimensional surface path (N/D) along which data was measured in cross-section A-A [6].

Out of all the different tests that were covered in the original technical report, the specific test case that was utilized for comparison with CFD in this thesis was test case AD462M-1, which was tested at Mach 8.08. AD462M-1 was selected for CFD comparison because of the laminar conditions, the circular leading edge, and the three lines normal to the leading edge along which data was measured, which meant more data for CFD validation. Many of the other test cases had induced turbulent flow by using a tripwire or sand paper, had a non-circular leading edge geometry, or used less than three lines of measurement.

The non-dimensional centerline locations of the three lines of pressure and heat-transfer measurements are specified in Table 4.1 with the geometric parameters of the AD462M-1 model. A SolidWorks model is shown in Figure 4.4 after Table 4.1 with body length to leading edge diameter ratio, or L/D. The sweep angle and color-coded lines where pressure and heat-transfer measurements were taken are also shown.

Table 4.1: AD462M-1 geometric configuration.

Sweep Angle	73°
Leading Edge Diameter (D)	1.02in
Body Length to Diameter Ratio (L/D)	16.0
Non-dimensional Centerline Locations (X/D)	7.85, 9.32, 12.28

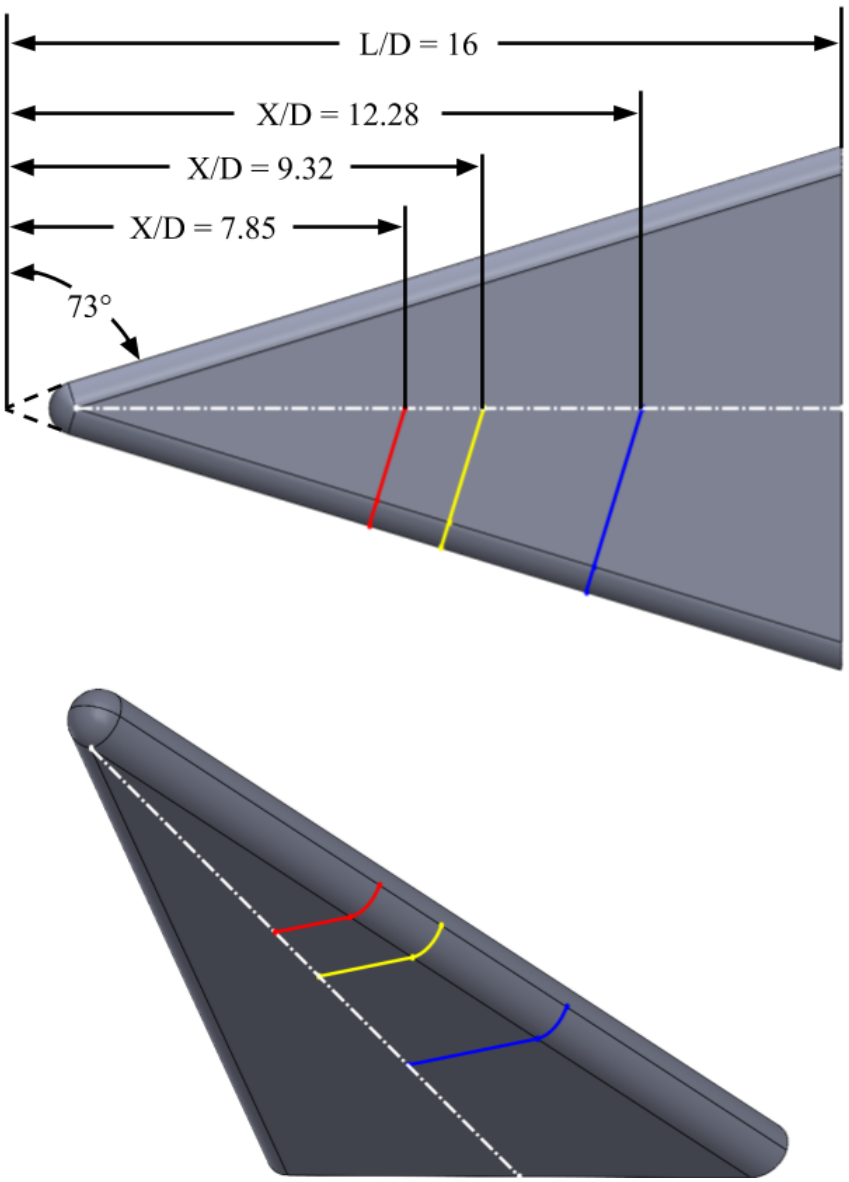

Figure 4.4: SolidWorks rendering of AD462M-1 model with non-dimensional centerline positions of lines along which pressure and heat transfer loads were measured [6], which are color coded for visual reference. White dashed line is the centerline.

The freestream conditions of the AD462M-1 wind tunnel test were published as stagnation conditions in the original report, so isentropic relations for compressible flow were utilized to determine the freestream static conditions of the test. These conditions are shown below in Table 4.2. Metric units were used for calculating the conditions since STAR-CCM+ is set up to work in metric units by default but the published stagnation freestream values in the report were in english units, so both english and metric units are shown in Table 4.2 for reference. Published values from the original report are denoted with an asterisk. The Reynolds number with respect to diameter that was calculated based on the freestream conditions does not exactly match the published value of 8.3×10^4 from the technical report, and it was not explained how the published freestream Reynolds number was obtained. It was decided to let the published stagnation conditions drive the freestream conditions rather than introduce further error or uncertainty from any altering of the published stagnation conditions in an attempt to get the right Reynolds number. Pressure and heat transfer measurements weren't collected at every angle of attack in the original test case but a full range from 0° to 30° in 5° increments covered both measurement sets.

Table 4.2: Freestream conditions for the AD462M-1 test [6]

Mach Number (M_∞)	8.08*
Stagnation Pressure (p_o)	200 psia* (1.38 MPa)
Stagnation Temperature (T_o)	1250° R* (694° K)
Static Pressure (p_∞)	0.0192 psia (132 Pa)
Static Temperature (T_∞)	88.9°R (49.4° K)
Density (ρ_∞)	5.83×10^{-4} lbm/ft^4 (9.34×10^{-3} kg/m^3)
Reynolds Number (Re_D)	8.7×10^4 (8.3×10^4)*

*original published value

The freestream isobaric specific heat of air was calculated from the polynomial in Equation 1.15 since it was not provided in the report. This value was required for calculating Stanton number in the CFD results. The initial temperature of the model and reference Stanton number were provided in the original report. All three of these refer-

ence values are in Table 4.3. Published values from the original report are denoted with an asterisk.

Table 4.3: Reference values for the AD462M-1 test [6].

Freestream Isobaric Specific Heat ($c_{p\infty}$)	1003 J/kg-K
Initial Model Temperature (T_i)	250° K (450° R)*
Reference Stanton Number (St_o)	0.0265

*original published value

4.2 Delta Wing Methodology

For the delta wing simulations, the solver settings and mesh settings from the validation case in Chapter 3 were utilized. The same approach of refining the circular leading edge of the delta wing as a function of it's leading edge diameter with minimum cell size was utilized as well. The only extra setting that was utilized was a wake refinement on the flat rear base of the delta wing by making the cell size twice the size of the cells on the leading edge. This was done to reduce cell count at the base since there was no region of interest that was being used for data comparison, so the level of refinement needed in that area did not need to be as high as the refinement on the leading edge. These mesh settings are shown in Table 4.4 below.

Table 4.4: Wake refinement options for flat base of the delta wing.

Wake Length Distance	1 leading edge diameter in length
Growth Rate	1.1
Cell Settings Controlled	Target and minimum surface size

The mesh was contained within a rectangular domain to model half of the delta wing. Like the hemisphere-cylinder simulations, there was also no need to have a large domain surrounding the model since the simulation was hypersonic, so long as shocks were not reflected off the surrounding domain surfaces. The domain was sized to clear the shocks coming off the body at all angles of attack. Space was given on the aft end of

the domain to resolve the overall wake structure as well. Because of the large rectangular proportions of the domain, body length (L) was used as the reference length for sizing the domain. The domain dimensions are in Figure 4.5 as a function of body length.

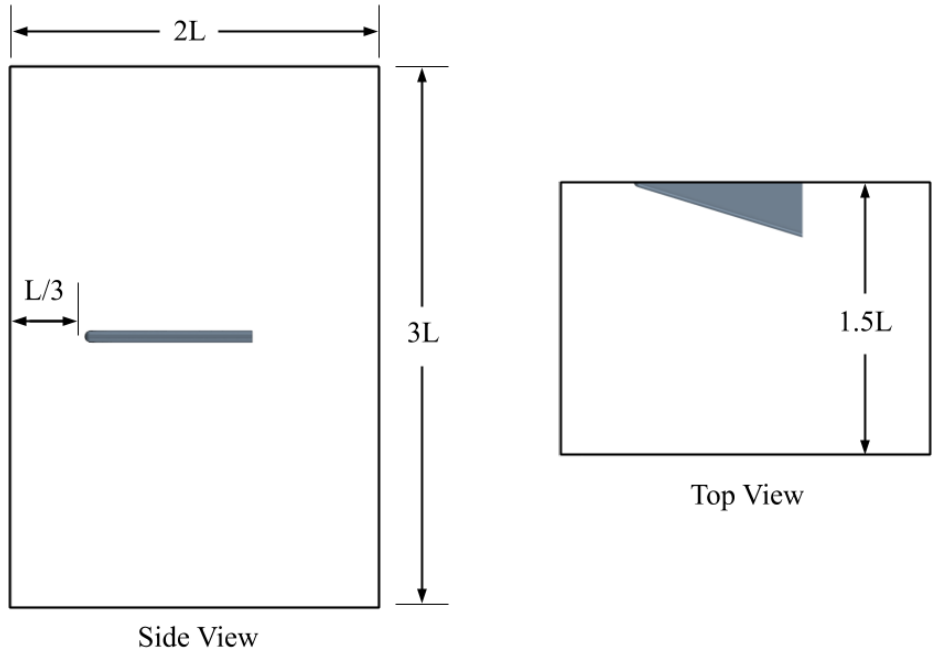

Figure 4.5: Side and top view of rectangular domain with dimensions in terms of body length.

4.3 Delta Wing Mesh Convergence Study

A mesh convergence study was performed at the highest angle of attack since this is where the overall heat transfer and aerodynamic force loads were expected to be the highest. The mesh convergence study was performed in the same fashion as the validation case with regards to refining the mesh as a percentage of the leading edge diameter. The same percentages of the leading edge diameter were used from the validation case, which were 8.7%, 7%, 5%, and 3%. Each mesh level required 45,000 iterations to reach convergence. The first prism layer cell height was calculated using equations 1.9 through 1.12 with an assumed $y+$ value of 0.1. The local Reynolds number was calculated with respect to the total length of the model which included half of the arc length of the leading edge. The

mesh settings for each level are listed in Table 4.5 below, with the first prism layer cell height being 7.16×10^{-7} m.

Table 4.5: Mesh levels used for mesh convergence study.

Mesh level	1	2	3	4
Minimum Cell Size	8.7%*	7%	5%	3%
Prism Layer Count	45	43	42	39
Total Prism Layer Thickness	15.7 mm	10.8 mm	9.1 mm	5.2 mm
Domain Cell Count	282,945	389,026	681,309	1,443,832

*default 36 points/circle value in STAR-CCM+

Mesh convergence was monitored in the same fashion as the validation case, which was done by looking at the relative change of net drag and heat transfer to the delta wing between mesh refinement levels. The only additional loads of convergence that were analyzed were lift and the normalized Stanton number at the three leading edge X/D locations.

The load values are listed in Table 4.6. The results showed that all relative change was within $\pm 1\%$ after level 2 for net lift, drag, and heat transfer. The normalized Stanton number had increased between 5% and 10% when going from level 1 to 2 at all leading edge X/D locations. From level 2 to 3, it increased by 1% at X/D = 7.85 and just over 3% at X/D = 9.32 and X/D = 12.28. Going from level 3 to 4 it increased by 1.3% at X/D = 7.85 but decreased by 0.6% and 2.6% percent at X/D = 9.32 and X/D = 12.28 respectively. Despite these fluctuations in relative change, mesh level 2 was selected for the delta wing simulations since the normalized Stanton number decreased after level 3 to fall within 0.5% to 2.8% of the values at level 2, as well as the fact that the net loads changed within $\pm 1\%$ of each mesh level after level 2. The relative change between mesh levels for normalized Stanton number and net loads is plotted in Figure 4.6 against cell count at the next mesh level, which in this case corresponds to cell count for level 2, 3 and 4 from left to right.

Table 4.6: Load values at each mesh level.

Mesh Level	1	2	3	4
Domain Cell Count	282,945	389,026	681,309	1,443,832
Net Lift	73.59 N	72.76 N (-1.1%)*	72.90 N (0.2%)*	73.12 N (0.3%)*
Net Drag	49.85 N	49.52 N (-0.7%)*	49.56 N (0.1%)*	49.48 N (-0.2%)*
Net Heat Transfer	614.9 W	618.3 W (0.6%)*	615.2 W (-0.5%)*	616.9 W (0.3%)*
Peak Normalized Stanton Number (X/D = 7.85)	0.2694	0.2833 (5.2%)*	0.2863 (1.1%)*	0.2901 (1.3%)*
Peak Normalized Stanton Number (X/D = 9.32)	0.2604	0.2744 (5.4%)*	0.2837 (3.4%)*	0.2820 (-0.6%)*
Peak Normalized Stanton Number (X/D = 12.28)	0.2521	0.2729 (8.3%)*	0.2817 (3.2%)*	0.2743 (-2.6%)*

*Relative change from previous mesh level

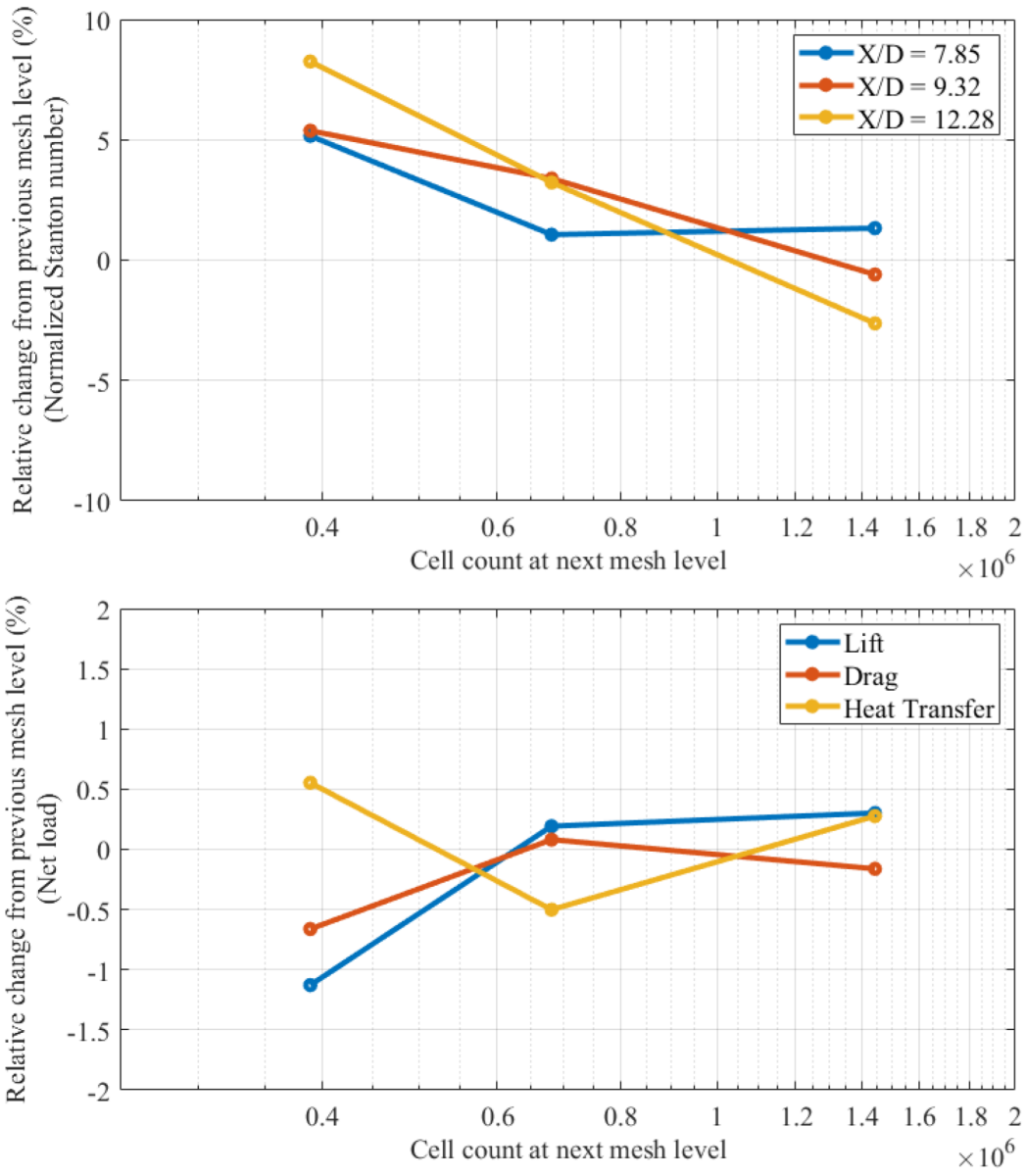

Figure 4.6: Convergence for normalized Stanton number and net lift, drag and heat-transfer.

To verify that the farfield walls were clear of any shocks at the highest angle of attack with the selected mesh level, contour scenes based on Mach number were generated onto the symmetry plane of the domain and on a horizontal cross section of the domain. It was shown that no shocks were in contact with the farfield walls. The symmetry plane contour scene is shown in Figure 4.7 and the horizontal cross section contour scene is shown in Figure 4.8.

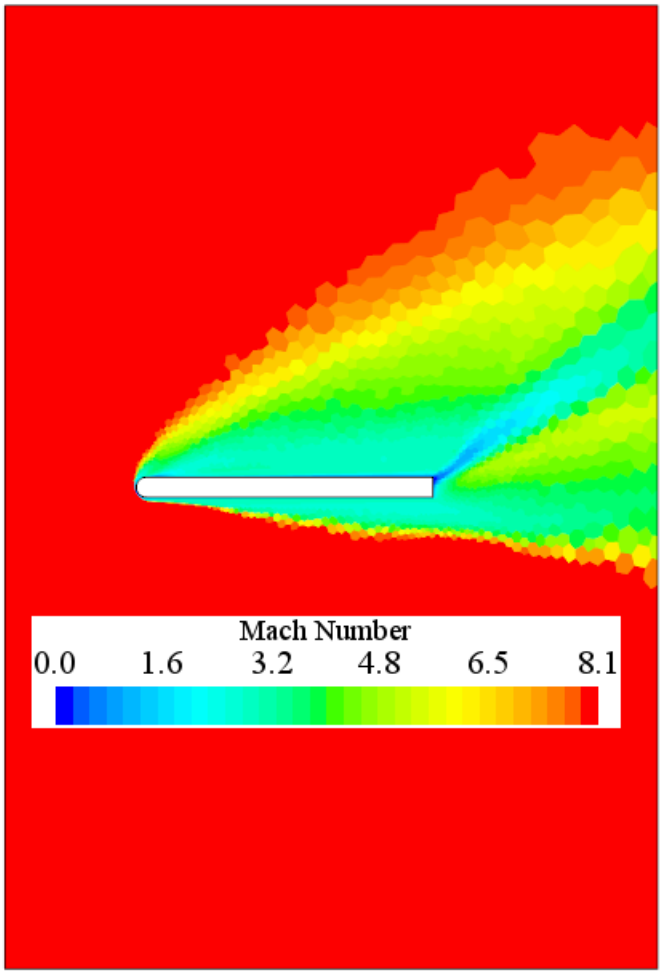

Figure 4.7: Contour scene of Mach number in the symmetry plane showing no shocks hitting the side boundaries of the farfield.

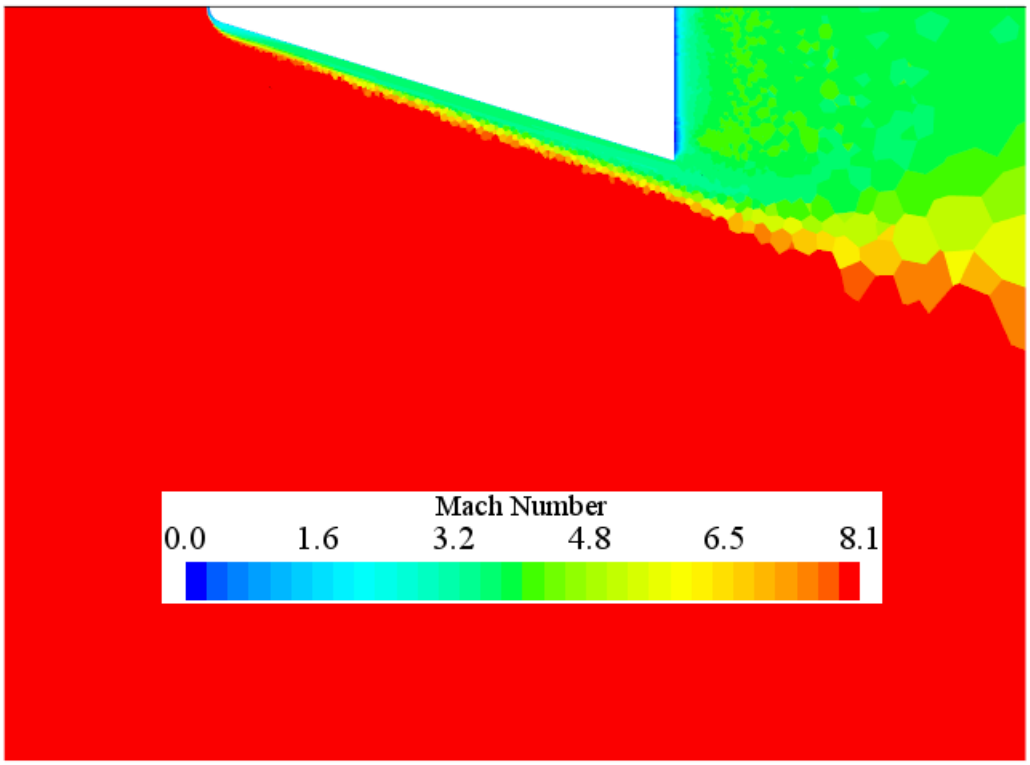

Figure 4.8: Contour scene of Mach number in the a horizontal cross section of the domain showing no shocks hitting the side boundaries of the farfield.

Figure 4.9 shows that $y+$ was less than 1 on the leading edge surface for a single turbulent case that was run with the selected mesh level. The case failed to run however with the original prism layer settings so the mesh was re-generated with a larger first prism layer height assuming a wall $y+$ of 1. This resulted in the first prism layer height being 7.16×10^{-6} with a total of 31 prism layer cells used and with a total prism layer height of 12.1 mm. However, the original mesh that assumed a $y+$ of 0.1 was used to run the laminar delta wing simulations to ensure that there was more than enough mesh resolution.

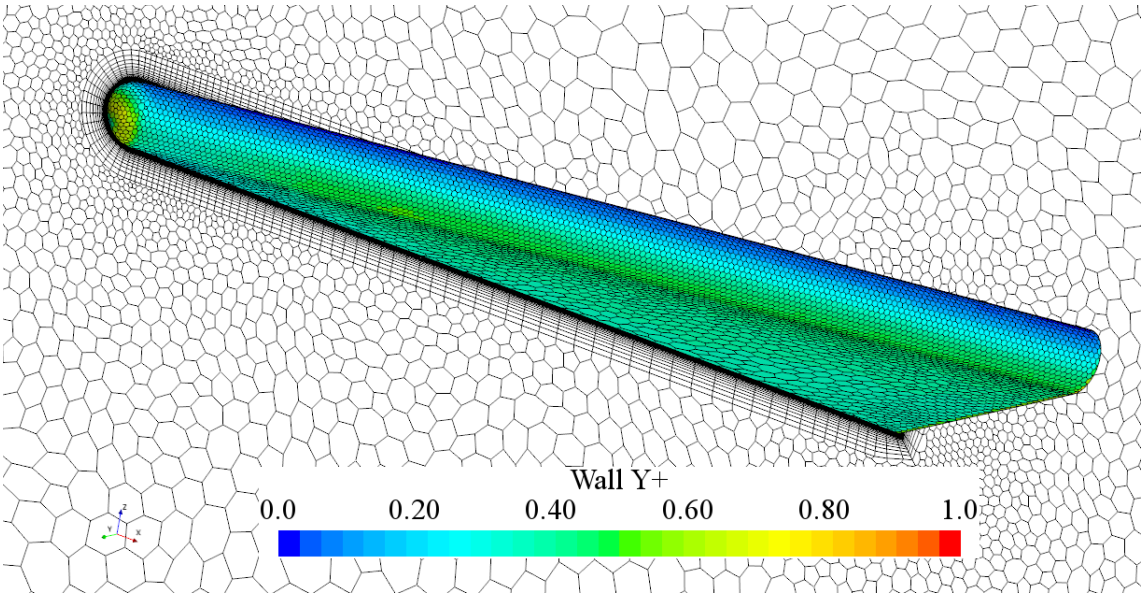

Figure 4.9: Turbulent case with the first prism layer size based on an assumed $y+$ of 1.

For the selected mesh level with laminar flow, the normalized Stanton number distribution was not scattered on the leading edge in the cross sectional plots, unlike the stagnation point of the hemisphere-cylinder. This was most likely attributed to the uniformity of the mesh that was achieved on the leading edge shown previously in Figure 4.9. The distributions of normalized Stanton number against the non-dimensional surface path on the leading edge are plotted in Figure 4.10. This individual case was run prior to running the rest of the cases in Section 4.4 to ensure that the distribution was smooth. The individual cell values are indicated with circles on the plotted lines for reference.

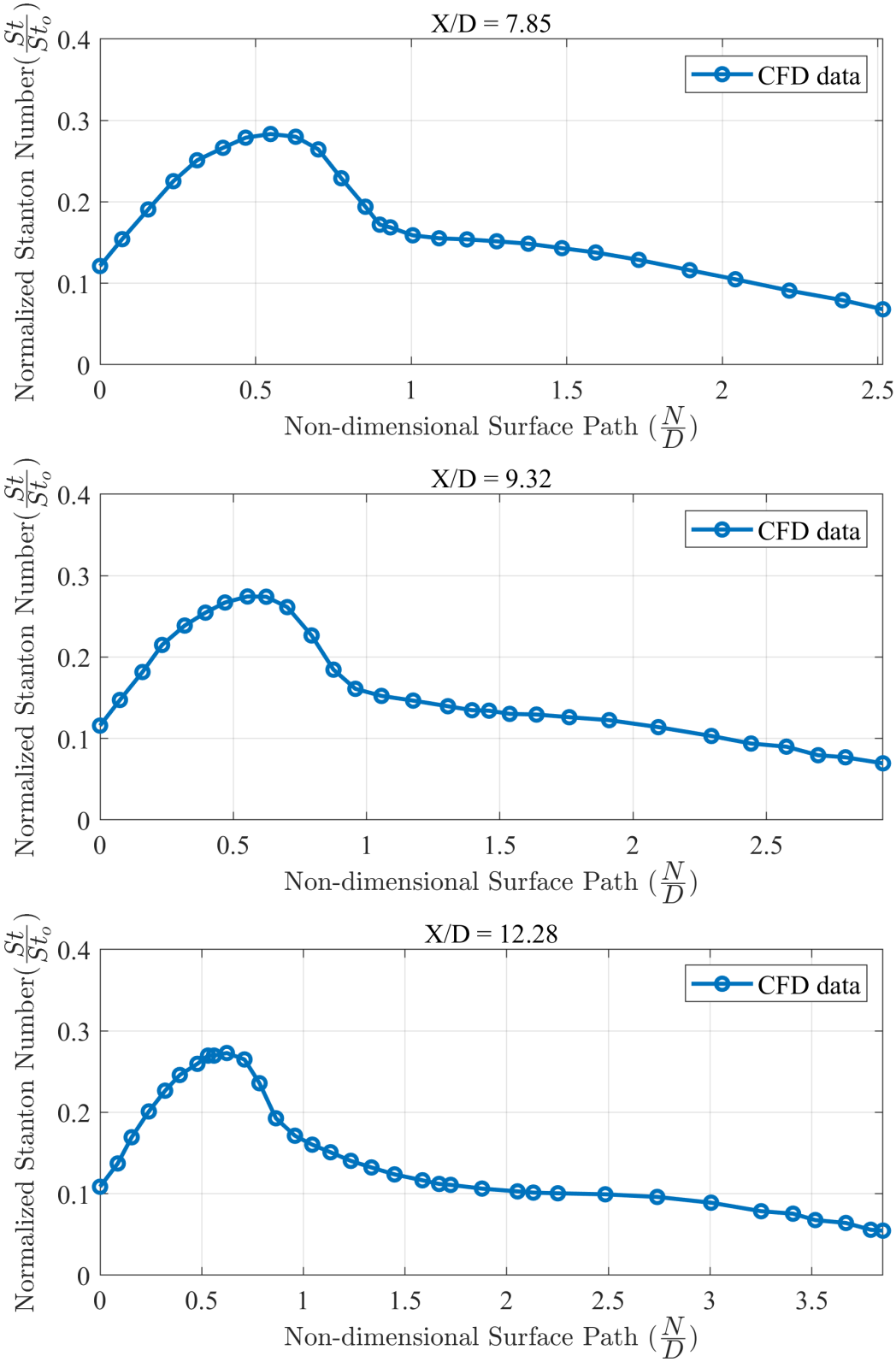

Figure 4.10: Normalized Stanton number against non-dimensional surface path.

4.4 Delta Wing Results

The peak normalized Stanton number was obtained at the three non-dimensional leading edge locations (X/D) of 7.85, 9.32, and 12.28 across the full range of angle of attack from 0° to 30°. Even though peak normalized Stanton number was available for just angles of attack 15° through 30° from the report, the CFD results for the lower angles of attack were plotted as well. Pressure coefficient wind tunnel data was compared to CFD as well. The plots in Figures 4.11, 4.12, and 4.13 show the peak heat transfer rate as normalized Stanton number plotted against the delta wing's angle of attack from both CFD and wind tunnel data as well as the percent error between them relative to the wind tunnel data. The observations specific to each case are made prior to each figure being introduced. The overall analysis and conclusions are then drawn in Section 4.5. Connecting the dots with the hemisphere-cylinder case is done in Chapter 5. The full collection of plots of normalized Stanton number against non-dimensional surface path and pressure coefficient against non-dimensional surface path is viewable in Appendix A.

The peak normalized Stanton number plotted against angle of attack is shown in Figure 4.11 at the non-dimensional leading edge location X/D = 7.85. The results show that there is a consistent overestimation in the predicted loads by at least 10% at every point. The error decreases as angle of attack increases up to 25° but reaches 17.4% at the highest angle of attack of 30°. The predicted loads both show a nearly linear load increase with angle of attack.

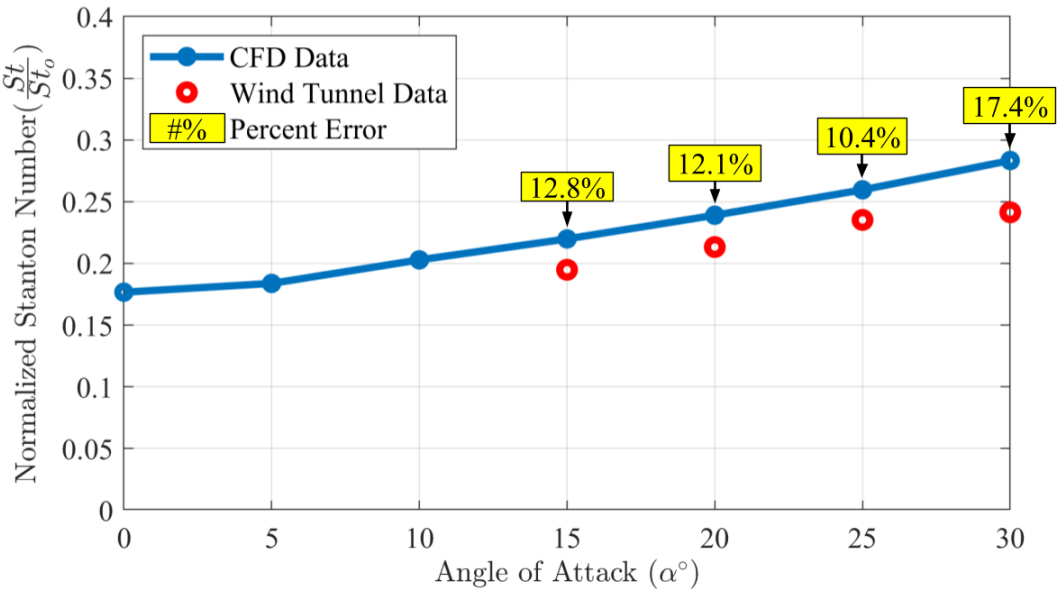

Figure 4.11: Peak normalized Stanton number vs angle of attack at non-dimensional leading edge location X/D = 7.85.

The peak normalized Stanton number plotted against angle of attack is shown in Figure 4.12 at the non-dimensional leading edge location X/D = 9.32. Relative to the previous results from the X/D = 7.85 location, there is also a consistent overestimate in the predicted loads but better agreement is shown since the overall percent error is smaller, with the largest percent error being 10.9% at an angle of attack of 20°. There is no decipherable trend in how the agreement changes as angle of attack changes. However, both CFD and wind tunnel data appear to capture the same overall trend in how the normalized Stanton number increases with angle of attack so far. This trend is observed in the previous location X/D = 7.85 in Figure 4.11.

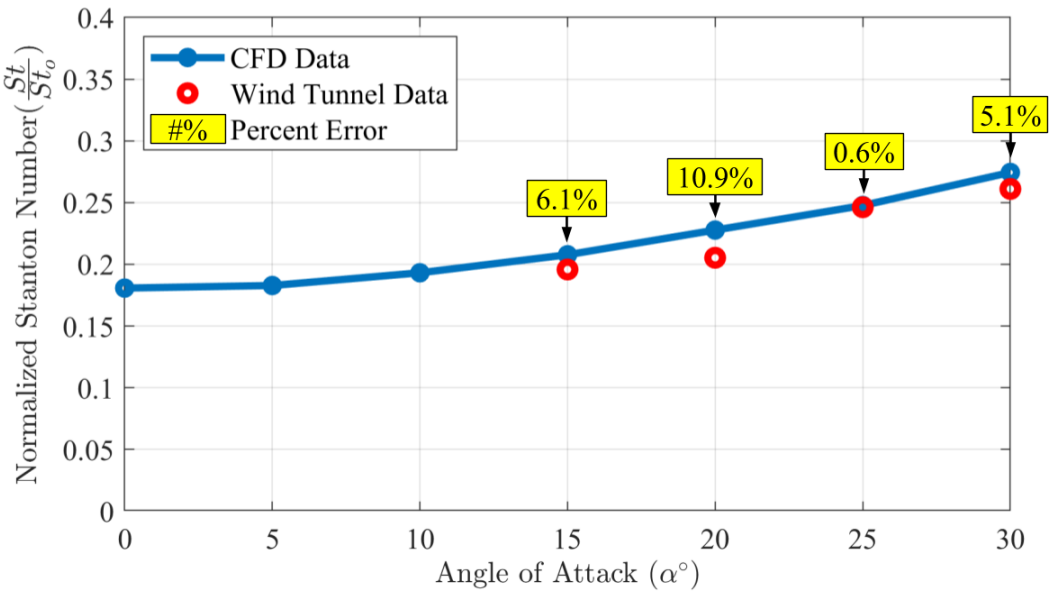

Figure 4.12: Peak normalized Stanton number vs angle of attack at non-dimensional leading edge location X/D = 9.32.

The peak normalized Stanton number against angle of attack is shown in Figure 4.13 at the non-dimensional leading edge location X/D = 12.28. Only three wind tunnel data points are plotted because the measured data that would have captured the peak normalized Stanton number for an angle of attack of 30° was not published at that condition. The peak normalized Stanton numbers at angles of attack of 20° and 25° are over predicted by 4.2% and 0.2% respectfully, but the third one at 15° is significantly under predicted by -18.8%. It is possible however that the largest error at an angle of attack 15° was due to error in measurement in the wind tunnel test. It can be inferred that the same trend in how normalized Stanton number changes with angle of attack is also observed at this leading edge location as the previous results in Figure 4.11 and Figure 4.12.

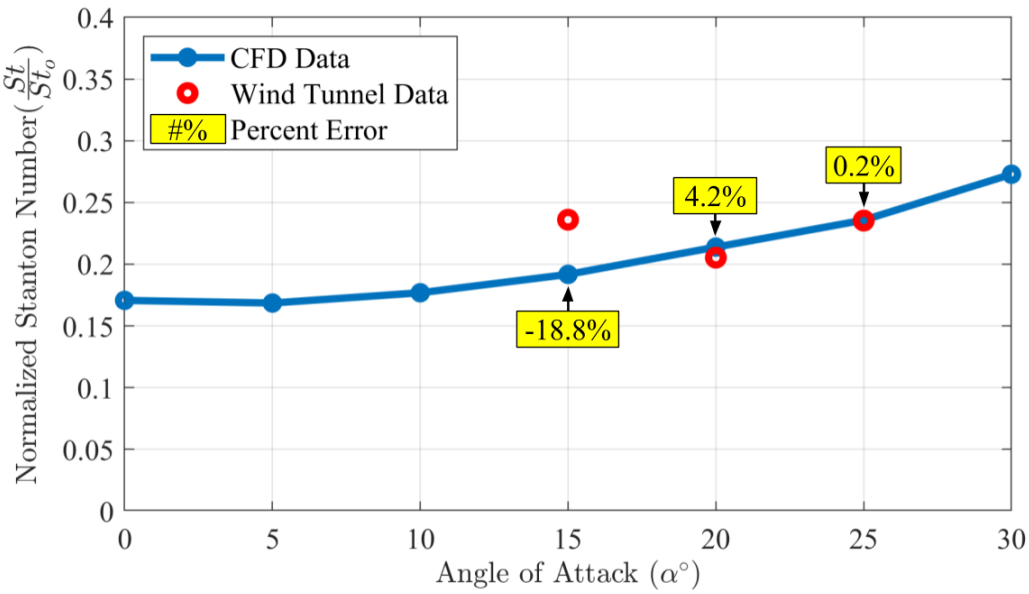

Figure 4.13: Peak normalized Stanton number vs angle of attack at non-dimensional leading edge location X/D = 12.28.

4.5 Delta Wing Discussion

The results from Figures 4.11 to 4.13 indicate that regardless of angle of attack, there is an overprediction of the heat transfer load towards the front tip of the delta wing between 10% to 20%, which is above the 6% maximum error of the wind tunnel data. This overprediction can be interpreted as a more adverse heat transfer load gradient on the leading edge of the wing moving from the frontal tip of the wing to one of the spanwise wing tips, which from a practical standpoint implies a higher thermal shock. Upon closer inspection of the leading edge, there is an area of higher normalized Stanton number just downstream of the front of the delta wing along the leading edge, which appears to be the culprit of the overprediction as shown in Figure 4.14 at an angle of attack of 30°. The dark red zone just upstream of the non-dimensional leading edge location X/D = 7.85 shows where the heat is concentrated.

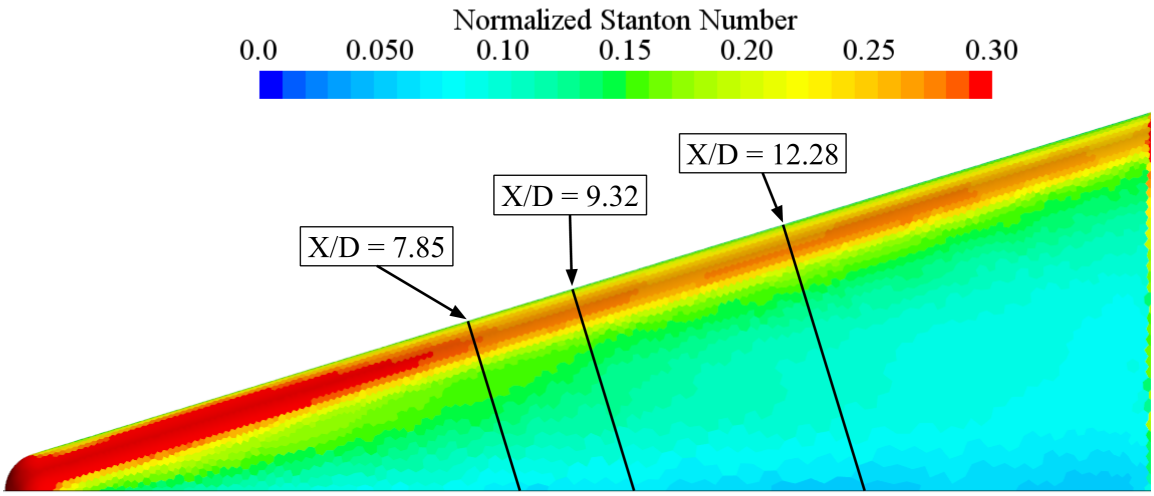

Figure 4.14: Normalized Stanton number with a gradient along the leading edge at an angle of attack of 30°.

Aside from the observed difference in heat transfer gradient along the leading edge, the normalized Stanton number predicted by CFD falls within ±20% of the wind tunnel data all around. The peak pressure values at the leading edge were not observed since most of the pressure taps were not closely placed enough to easily detect the peak. Regardless, the wind tunnel pressure tap measurements that were closest to the stagnation point in CFD predicted agreed within ±10% of the pressure coefficient that CFD predicted at their specific location. This was observed across all angles of attack that had published pressure coefficient data for all three non-dimensional leading edge locations.

Chapter 5

DISCUSSION

The most important observation is that the hemisphere-cylinder and delta wing CFD cases exhibited different behaviors with regards to overpredicting the heat transfer loads. The hemisphere-cylinder exhibited a large overprediction in heat transfer load at the stagnation point of the hemisphere face by 21.8%. The region of overprediction in heat transfer also happened to be where subsonic flow surrounded the stagnation point, but everything downrange of this region saw much better qualitative agreement. The peak heat transfer loads on the delta wing leading edge were also overpredicted but the error was between 10% to 20% on the leading edge location that was closest to the front of the wing. The error was reduced to below 10% on the leading edge location that was furthest from the front, with the exception of one case at an angle of attack of 15° that was off by -18.8%. The overall observations from both cases implies that STAR-CCM+ can resolve the heat transfer loads in regions that are not fully stagnant better than regions that are fully stagnant with an ideal gas model in laminar flow. The ideal gas model does not take into account the effects that a multi-species gas would predict in regions of stagnant flow where temperature is the highest. The gas properties that would have an impact on the local heat transfer loads such as ratio of specific heats, viscosity, and thermal conductivity are not just based on temperature in a multi-species gas but also on the chemical makeup of the gas. This is a likely culprit for the larger overprediction in the heat transfer on the stagnation point of the hemisphere-cylinder.

Mesh quality was a contributor to the uniformity of the results for both the hemisphere-cylinder and delta wing cases. The hemisphere part of the hemisphere-cylinder showed variation in heat transfer load at cells that shared the same x-coordinate location

while the loads on the cylinder surface downstream were nearly the same at every cell that had the same x-coordinate. This was due to the non-uniform surface mesh that was generated on the hemisphere surface, while the surface mesh on the cylinder surface downstream was generated with a uniform pattern. The variation of heat transfer on the hemisphere face was most likely not due to the selected solver or physics settings failing to resolve the flow because past the subsonic region the heat transfer loads on the hemisphere face had qualitatively better agreement than the heat transfer loads right at the stagnation point. The delta wing leading edge however had a uniform surface mesh pattern and the plots showing normalized Stanton number against non-dimensional surface path showed smooth and continuous distributions of heat transfer.

For the hemisphere-cylinder, the 2D axisymmetric case failed to resolve the heat transfer load for the two cells that were closest to the stagnation point, resulting in an overprediction of the peak heat transfer load by 383%. The peak heat transfer load away from the stagnation point was overpredicted by 36%. The 3D case produced results that were off by only 21.8% at the stagnation point, and the CFD results agreed with the wind tunnel data much better from a qualitative standpoint. This suggests that the physics settings selected for this thesis may not be appropriate for 2D axisymmetric STAR-CCM+ hypersonic CFD simulations, specifically when using the ideal gas model in laminar flow near stagnation points. Since a more refined mesh failed to converge for the 2D case, a higher order method of modeling the gas such as the multi-species gas model used by Cross and West [12] might be necessary.

The error margin from STAR-CCM+ overpredicting the heat transfer loads near the stagnation point was approximately 20% which is well above the 4.5% and 6% error associated with the wind tunnel data for the hemisphere-cylinder and delta wing cases, respectfully. However, the largest error seen in the delta wing case was from the most downstream location on the delta wing leading edge at an angle of attack of 15°, where

the wind tunnel data was 18.8% higher than the CFD results. This heat transfer load from the wind tunnel data was suspiciously high since the peak heat transfer loads at the higher angles of attack were lower, implying that there was larger error associated with some portions of the published wind tunnel data.

Both of the cases studied in this thesis were sufficiently mesh-converged with a very low mesh resolution each under 2 million cells. While previous work done by Cross and West [12] was in 2D, the equivalent level of mesh refinement they used would have resulted in a 3D mesh with many millions of cells. This suggests that the ideal gas model in laminar flow with temperature-dependent isobaric specific heat, viscosity, and thermal conductivity requires a mesh refined enough to capture primarily viscous effects for heat-transfer loads that are near the leading edge surfaces, which implies regions of attached flows. The regions downstream of the leading edge of the delta wing were not analyzed and no specific mesh control was used to govern the mesh resolution. These downstream regions have highly separated or more stagnant flow depending on if the top or bottom of the delta wing is analyzed. Based on the work by Cross and West [12], a study of the loads within the separated region would require a much more refined mesh that may be better suited with adaptive mesh refinement.

Predicting pressure loads was not necessarily part of the thesis objective, but the pressure distributions on the delta wing leading edge did see good agreement near the peak pressure coefficient, with no more than $\pm 10\%$ error. This is good confirmation of the functionality of STAR-CCM+ for predicting pressure distributions in hypersonic flow since Newtonian Theory discussed in Section 1.2 shows that predicting hypersonic flow pressure loads should be an easy process.

The cell count being no larger than 2 million did not necessarily mean that results were less computationally expensive. For the delta wing cases, the required 45,000 iterations to reach a converged stage for heat transfer loads offset the potential reduction in

computational expense of using meshes with low cell count. This resulted in CFD simulations running for longer periods of time than anticipated.

Chapter 6

CONCLUSIONS AND FUTURE WORK

STAR-CCM+ CFD simulations were run on a hemisphere-cylinder and delta wing at steady-state hypersonic conditions in laminar flow. The purpose was to verify that the chosen physics settings and meshing practices were valid for predicting heat transfer loads on forward-facing surfaces in STAR-CCM+. The hemisphere-cylinder was run at Mach 6.74 with a focus in analyzing the heat transfer load near the stagnation point, while the delta wing was run at Mach 8.08 from an angle of attack of 0° to 30° in increments of 5° with a focus in analyzing the peak heat-transfer loads on the swept leading edge. The physics settings for both cases utilized an ideal gas model with variable isobaric specific heat, viscosity, and thermal conductivity all as functions of temperature. Since these properties were only dependent on temperature for a single species gas, the effects that a multi-species gas would have on these properties at higher temperatures were not taken into account.

Mesh convergence studies were performed for the hemisphere-cylinder and delta wing CFD simulations by increasing the number of surface cells on the leading edge. Mesh convergence was monitored by observing the pressure and heat transfer load values across four levels of mesh refinement. All monitored loads for the selected levels of mesh refinement for both the hemisphere-cylinder and delta wing simulations were within $\pm 3\%$ of the loads from the highest level of mesh refinement.

The largest error in STAR-CCM+ CFD results relative to wind tunnel data was on the order of $\pm 20\%$ for both the hemisphere-cylinder and delta wing simulations. Most of the larger error in the simulations was due to overpredictions in the heat transfer loads. The hemisphere-cylinder case showed that in hypersonic STAR-CCM+ simulations the quality

of the surface mesh has an impact on the uniformity of the distribution of heat transfer loads, but not necessarily the overall accuracy of the results. This issue was avoided in the delta wing simulations because the leading edge surface mesh had a uniform mesh pattern.

The NASA report goes over many other test configurations of delta wing geometries with different diameters, length to body ratios, sweep angles, as well as different leading edge curvatures. The technical report is very detailed in describing the other configurations that were analyzed and how the results of the different configurations of the delta wings compared to each other. This leaves a lot of open-ended questions as to how well STAR-CCM+ can capture hypersonic pressure and heat transfer loads with variation of geometry parameters such as sweep angle and leading edge curvature on a delta wing. The other geometry configurations of the delta wing were not covered in this thesis because the focus was to verify that the chosen physics settings and meshing practices were valid for predicting heat transfer loads on forward-facing surfaces in STAR-CCM+, hence why both the hemisphere-cylinder and delta wing simulations were run with the same settings and practices.

Multi-species gas modeling would be an appropriate next step to help confirm that the overestimation in heat transfer loads from this thesis is due to the utilization of an ideal gas model with only temperature-dependent effects on the gas properties. The work by Cross and West [12] goes into detail on how to utilize the multi-species modeling in STAR-CCM+ for both laminar and turbulent flows. It must be kept in mind that it is much more computationally expensive to simulate a multi-species gas. Not just in terms of more computations to compute per cell, but also with regards to the possibility of needing an adaptive mesh refinement technique to refine areas that capture shockwaves in the flow field.

BIBLIOGRAPHY

[1] Jonathan Strickland. "How the Apollo Spacecraft Worked", January 2020. https://science.howstuffworks.com/apollo-spacecraft7.htm.

[2] Antonio Viviani. *Aerodynamic and Aerothermodynamic Analysis of Space Mission Vehicles*. Springer International Publishing Switzerland, 2015.

[3] "NASA Dryden Fact Sheets - X-15 Hypersonic Research Program", August 2015. https://www.nasa.gov/centers/armstrong/news/FactSheets/FS-052-DFRC.html.

[4] Jason C. Engle. "Dyna-Soar (X-20)". https://www.afmc.af.mil/Portals/13/DynaSoar.pdf.

[5] Henry C. Dethloff. "The Space Shuttle's First Flight: STS-1". https://history.nasa.gov/SP-4219/Chapter12.html.

[6] A.L. Nagel, H.D. Fitzsimmons, and L.B. Doyle. "Analysis of Hypersonic Pressure and Heat Transfer Tests on Delta Wings with Laminar and Turbulent Boundary Layers Final Report", August 1966. https://ntrs.nasa.gov/citations/19660026816.

[7] "Dryden History - The Lifting Bodies - Bill Dana", August 1966. https://www.nasa.gov/centers/dryden/history/Speeches/lifting_bodies/lifting-1.html.

[8] "Boundary Layer Transition". https://www.theairlinepilots.com/forumarchive/principlesofflight/boundarylayer.jpg.

[9] "Automatic (CFD) for the People", May 2020. https://blogs.sw.siemens.com/simcenter/aerodynamic-database-generation-with-cfd/.

[10] VL Srinivas. "Shape Optimization of a Car Body for Drag Reduction and to Increase Downforce", April 2016. https://www.researchgate.net/publication/301673979_Shape_Optimization_of_a_Car_Body_for_Drag_Reduction_and_to_Increase_Downforce.

[11] "Law of the Wall". https://www.cfd-online.com/Wiki/Law_of_the_wall.

[12] Peter Cross and Michael West. "Simulation of Hypersonic Flowfields Using STAR-CCM+", Jan 2019. https://apps.dtic.mil/dtic/tr/fulltext/u2/1069198.pdf.

[13] Eli Ray Shellabarger. "Computational Characterization of Shock Wave - Boundary Layer Interactions on Flat Plates and Compression Ramps in Laminar, Hypersonic Flow", 2018. https://lib.dr.iastate.edu/etd/16465/.

[14] Ryan Wood. "Hypersonic Boundary Layer Behaviour in Mach 6 Flow Over a Non-Uniformly Heated Flat Plate", 2018. https://ojs.unsw.adfa.edu.au/index.php/juer/article/view/1134.

[15] Nathan Richardson. "STAR-CCM+ Hypersonic Validation of a 70° Sweep Slab". https://mdx2.plm.automation.siemens.com/presentation/star-ccm-hypersonic-validation-70%C2%B0-sweep-slab.

[16] Davis H. Crawford and William D. McCauley. "Investigation of the laminar aerodynamic heat-transfer characteristics of a hemisphere-cylinder in the Langley 11-inch hypersonic tunnel at a Mach number of 6.8", 1957. https://ntrs.nasa.gov/citations/19930092313.

APPENDICES

Appendix A

DELTA WING DATA

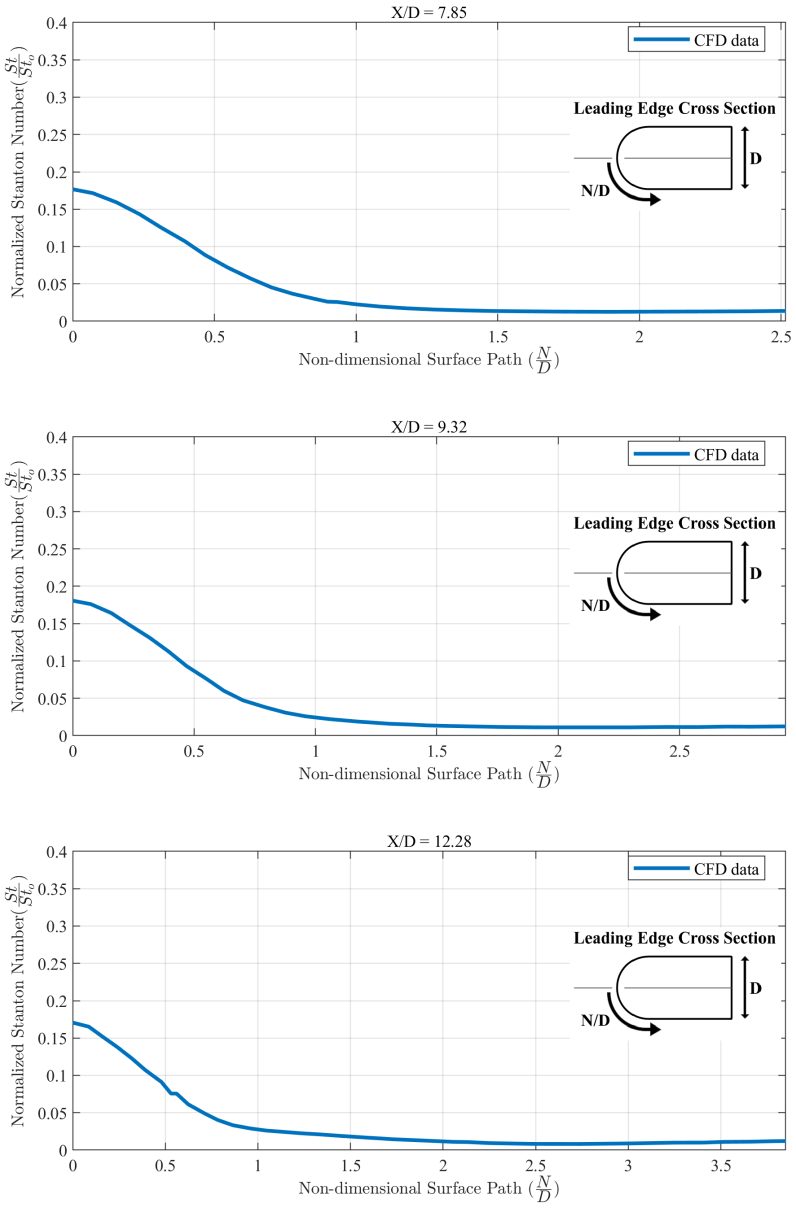

Figure A.1: Normalized Stanton number against non-dimensional surface path for angle of attack 0° at non-dimensional leading edge locations 7.85, 9.32, and 12.28.

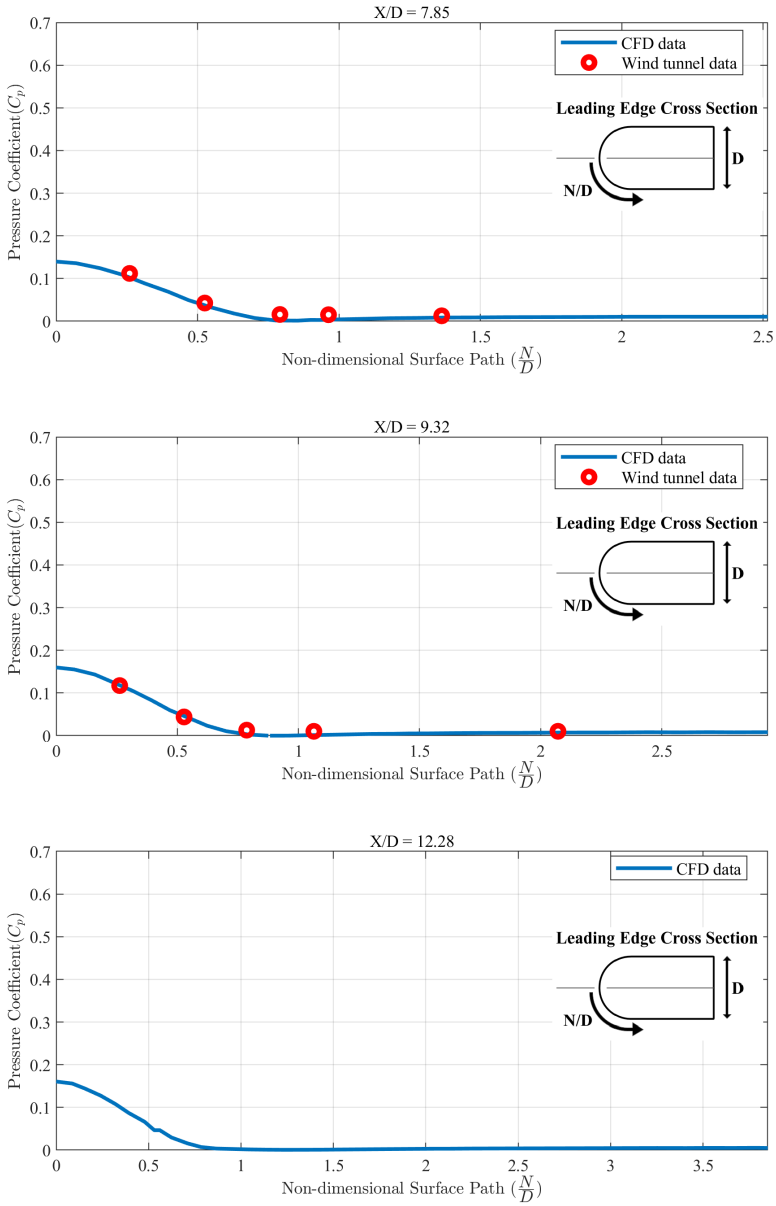

Figure A.2: Pressure coefficient against non-dimensional surface path for angle of attack 0° at non-dimensional leading edge locations 7.85, 9.32, and 12.28.

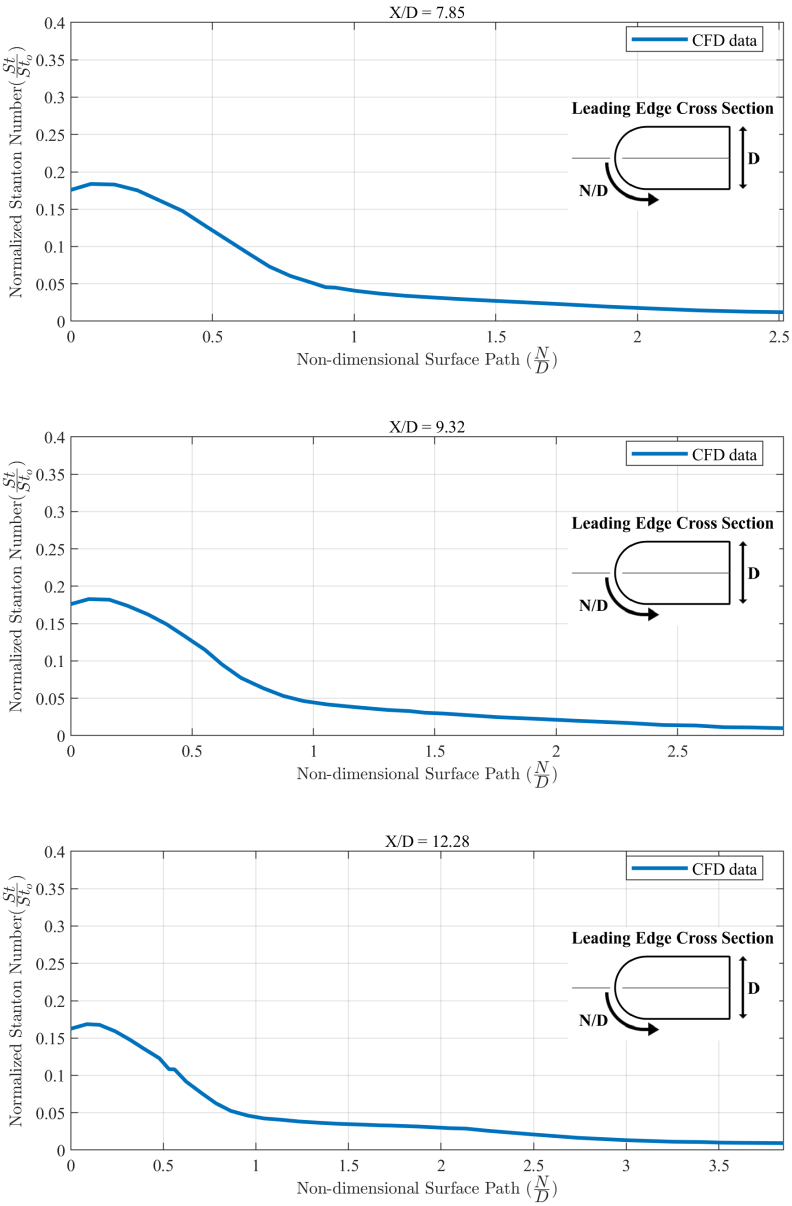

Figure A.3: Normalized Stanton number against non-dimensional surface path for angle of attack 5° at non-dimensional leading edge locations 7.85, 9.32, and 12.28.

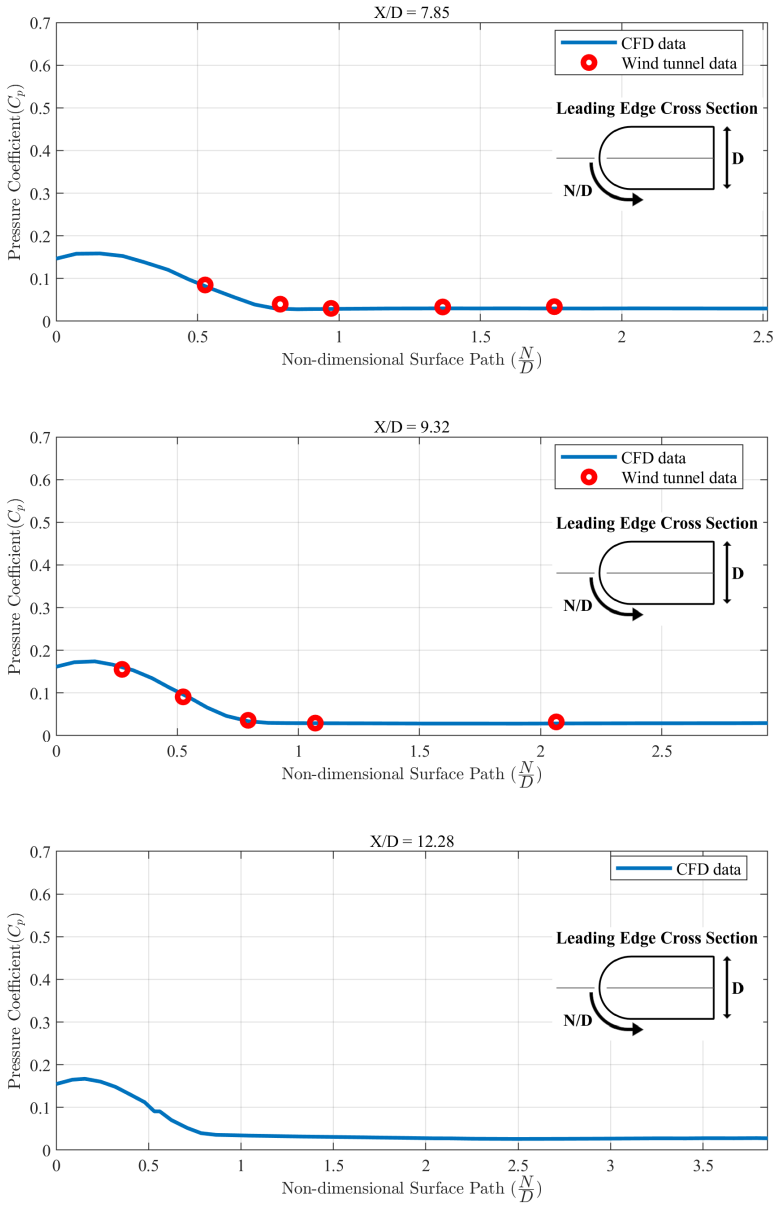

Figure A.4: Pressure coefficient against non-dimensional surface path for angle of attack 5° at non-dimensional leading edge locations 7.85, 9.32, and 12.28.

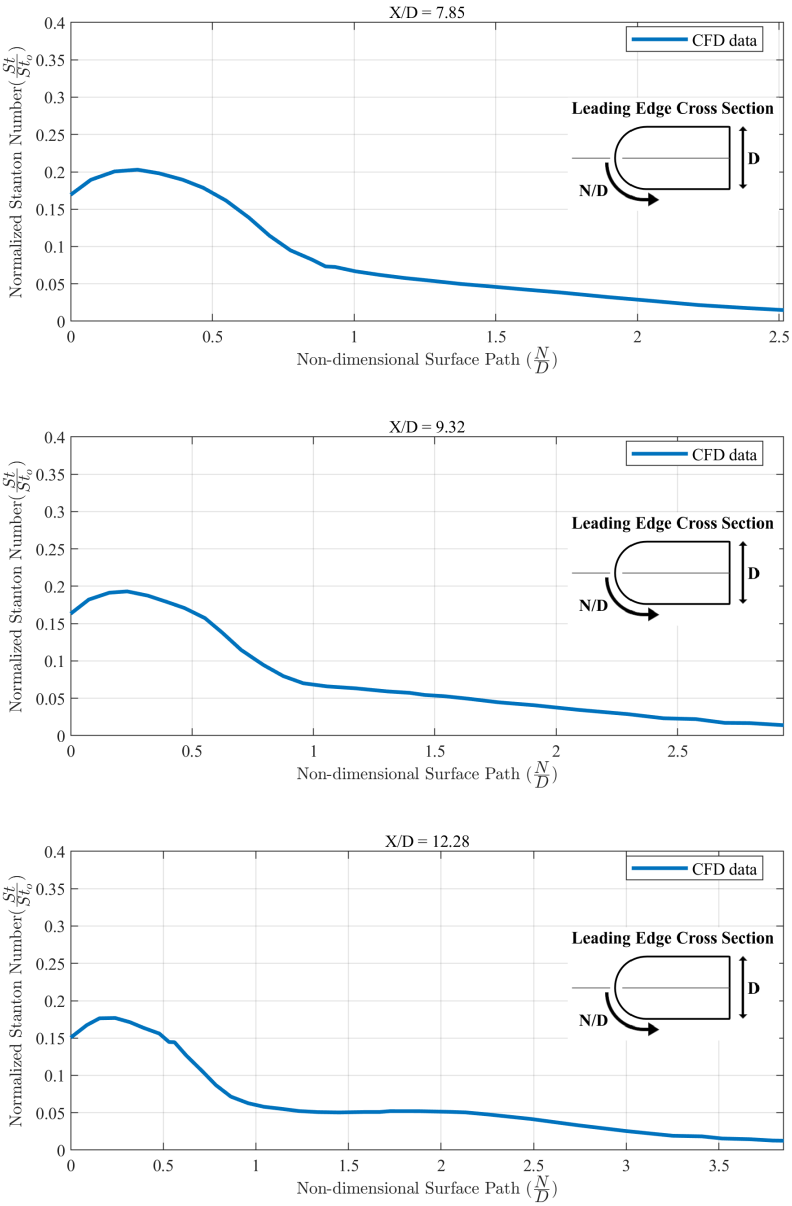

Figure A.5: Normalized Stanton number against non-dimensional surface path for angle of attack 10° at non-dimensional leading edge locations 7.85, 9.32, and 12.28.

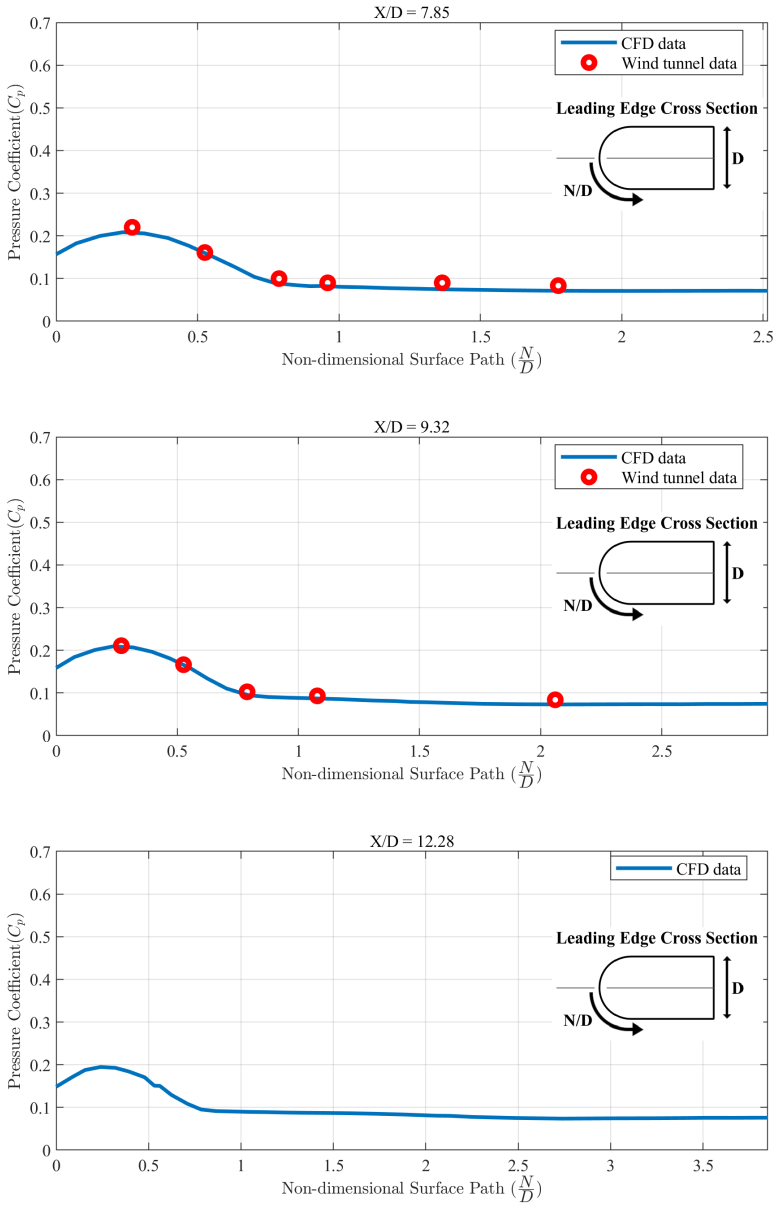

Figure A.6: Pressure coefficient against non-dimensional surface path for angle of attack 10° at non-dimensional leading edge locations 7.85, 9.32, and 12.28.

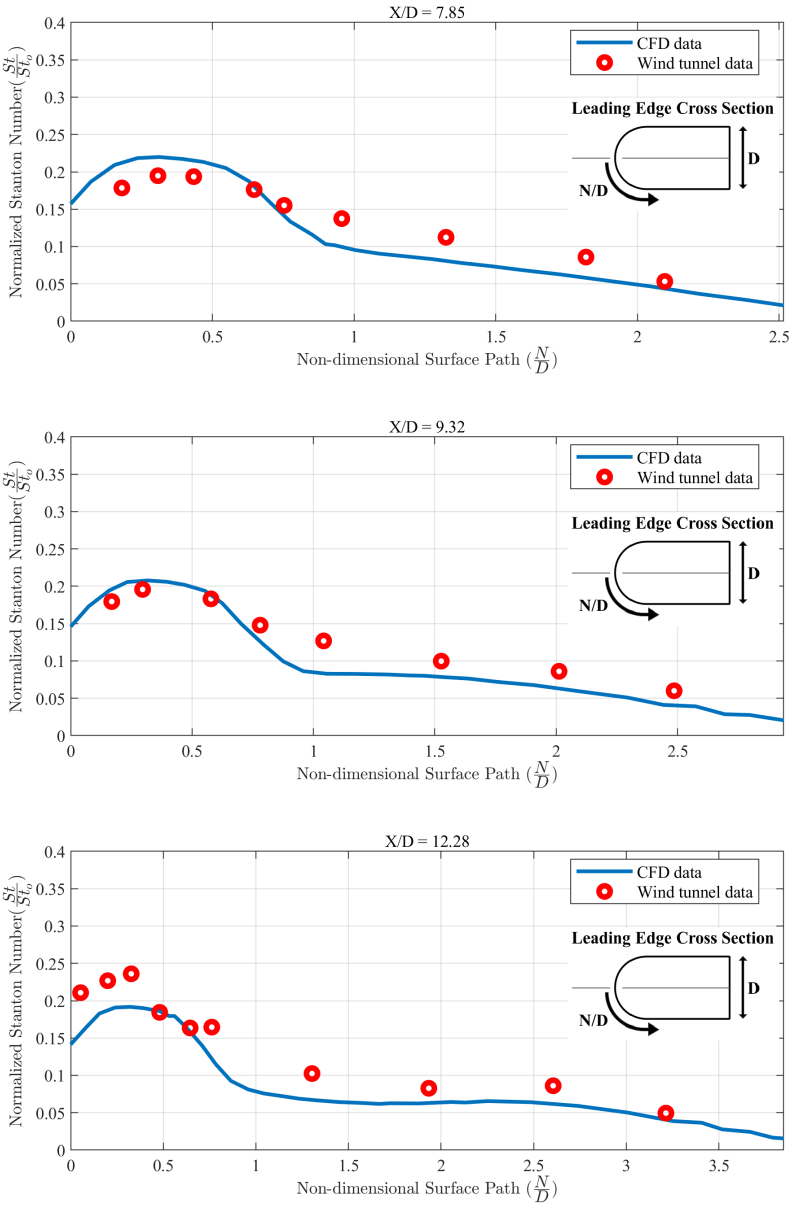

Figure A.7: Normalized Stanton number against non-dimensional surface path for angle of attack 15° at non-dimensional leading edge locations 7.85, 9.32, and 12.28.

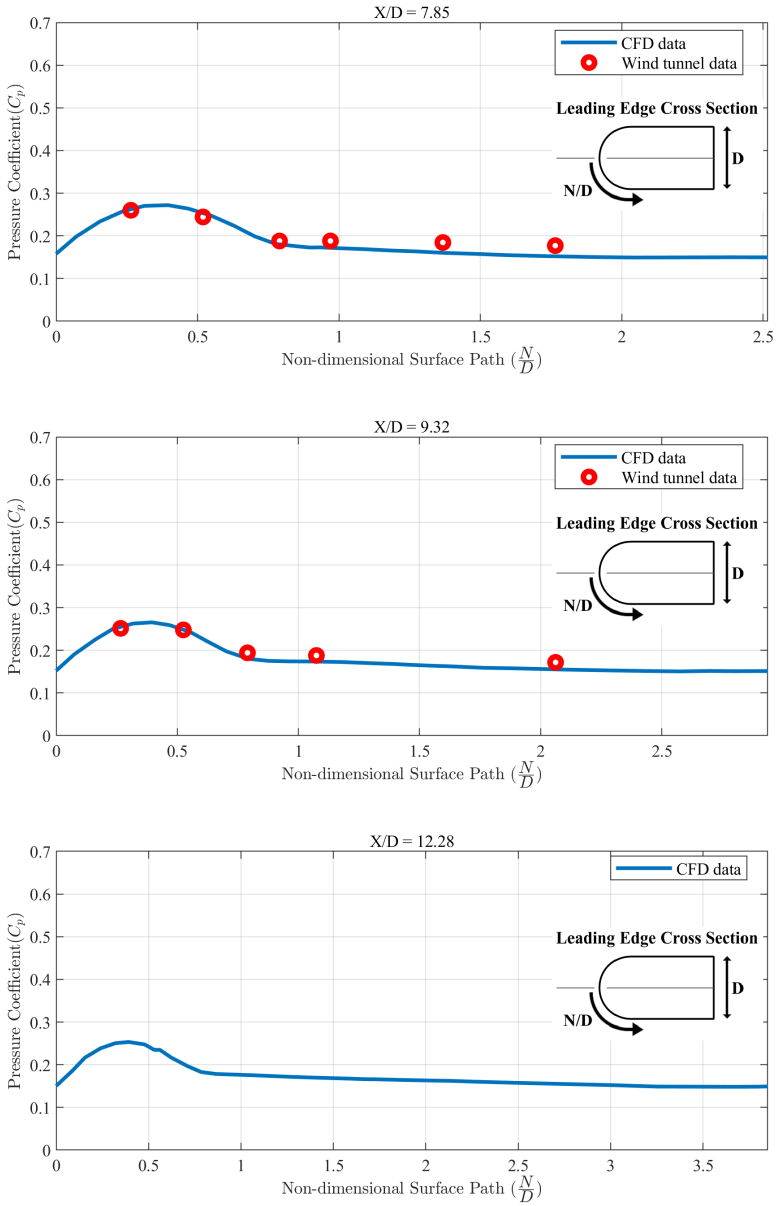

Figure A.8: Pressure coefficient against non-dimensional surface path for angle of attack 15° at non-dimensional leading edge locations 7.85, 9.32, and 12.28.

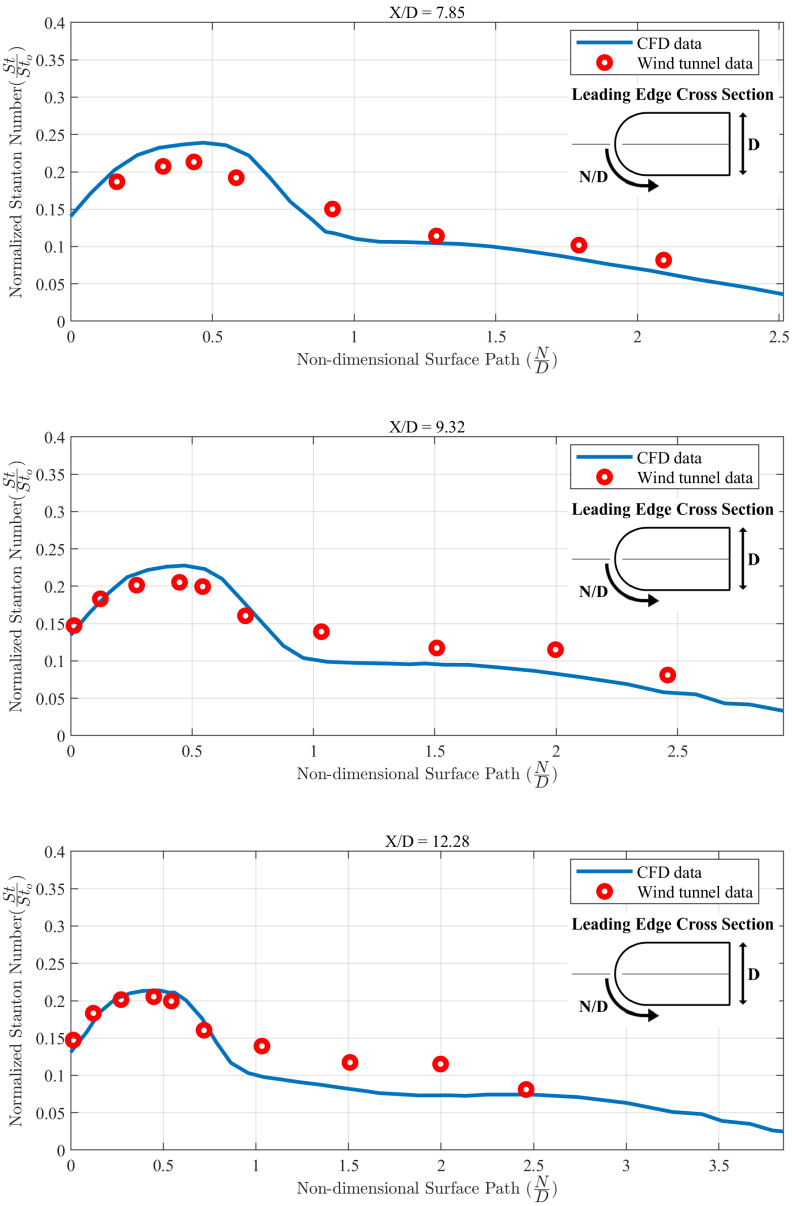

Figure A.9: Normalized Stanton number against non-dimensional surface path for angle of attack 20° at non-dimensional leading edge locations 7.85, 9.32, and 12.28.

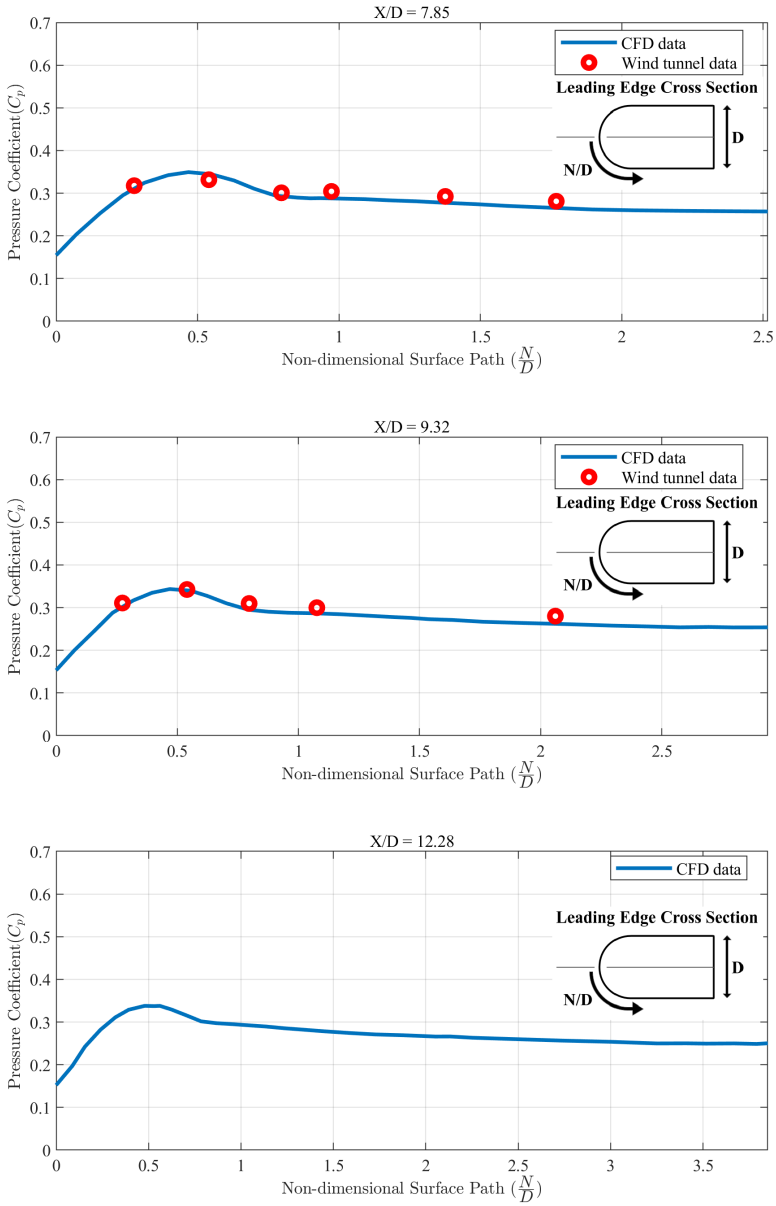

Figure A.10: Pressure coefficient against non-dimensional surface path for angle of attack 20° at non-dimensional leading edge locations 7.85, 9.32, and 12.28.

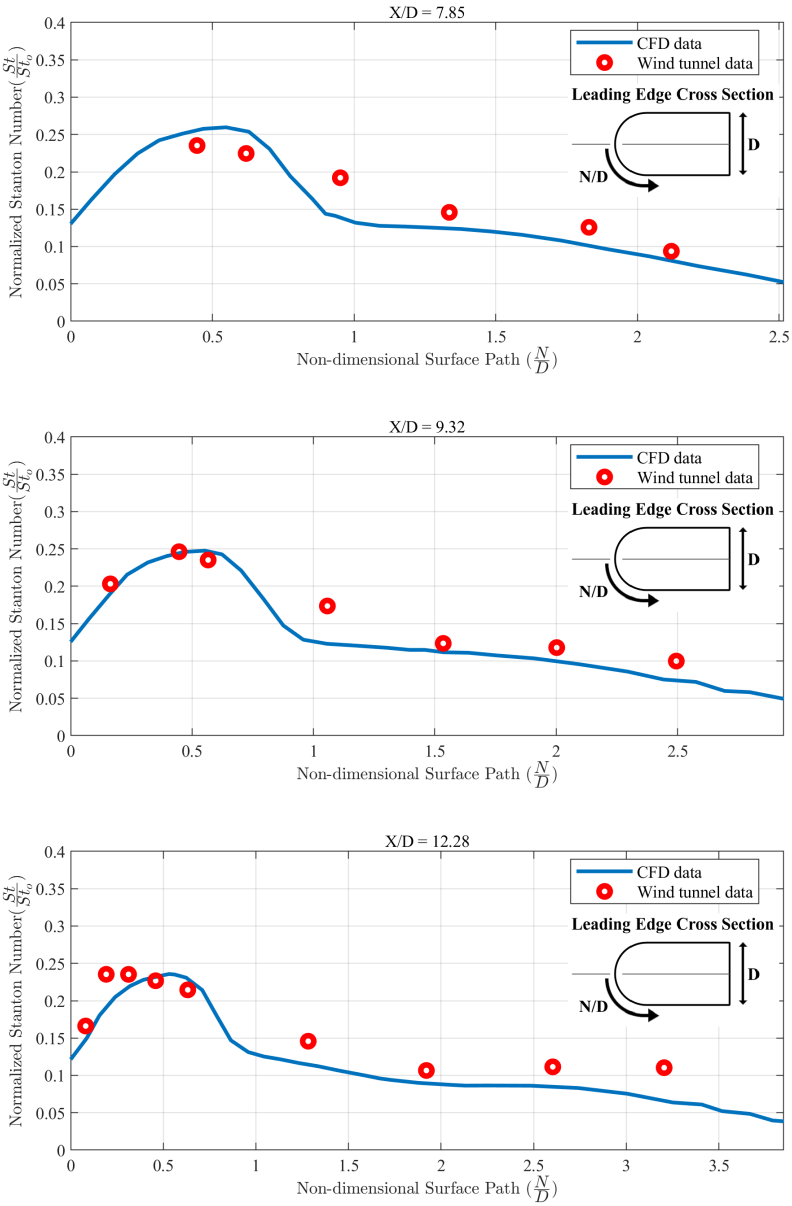

Figure A.11: Normalized Stanton number against non-dimensional surface path for angle of attack 25° at non-dimensional leading edge locations 7.85, 9.32, and 12.28.

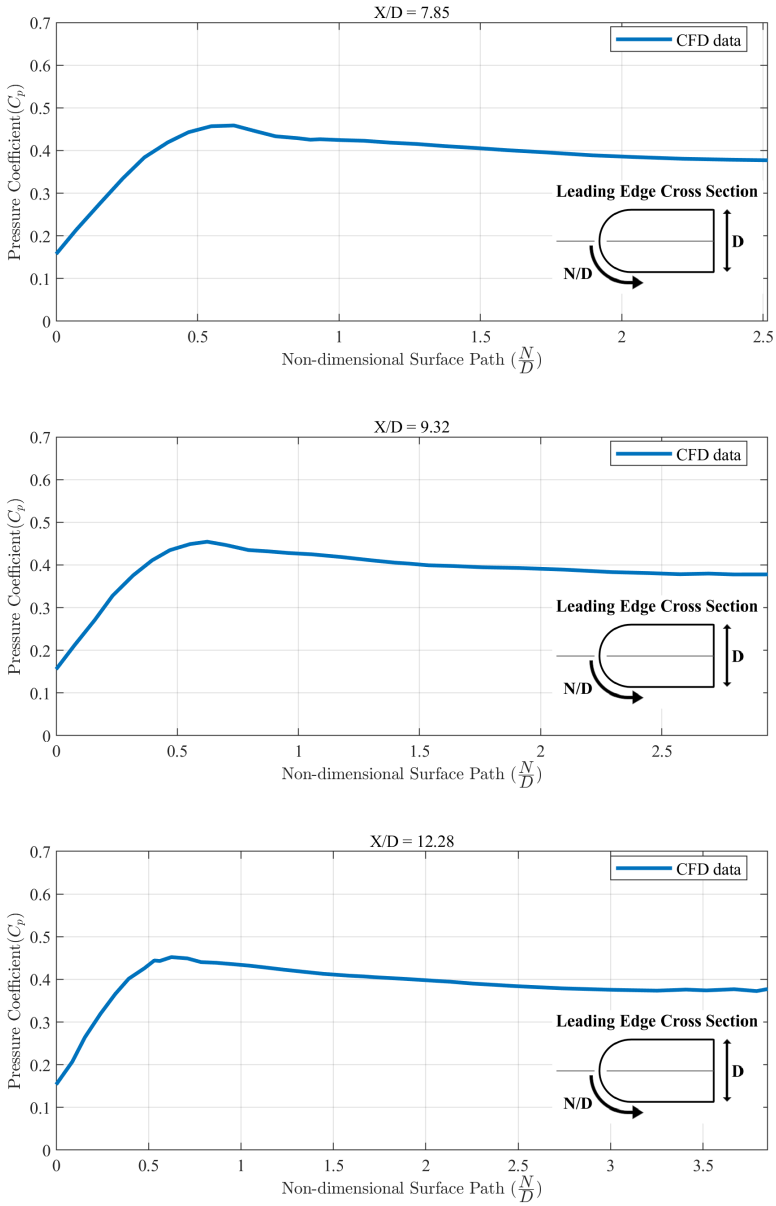

Figure A.12: Pressure coefficient against non-dimensional surface path for angle of attack 25° at non-dimensional leading edge locations 7.85, 9.32, and 12.28.

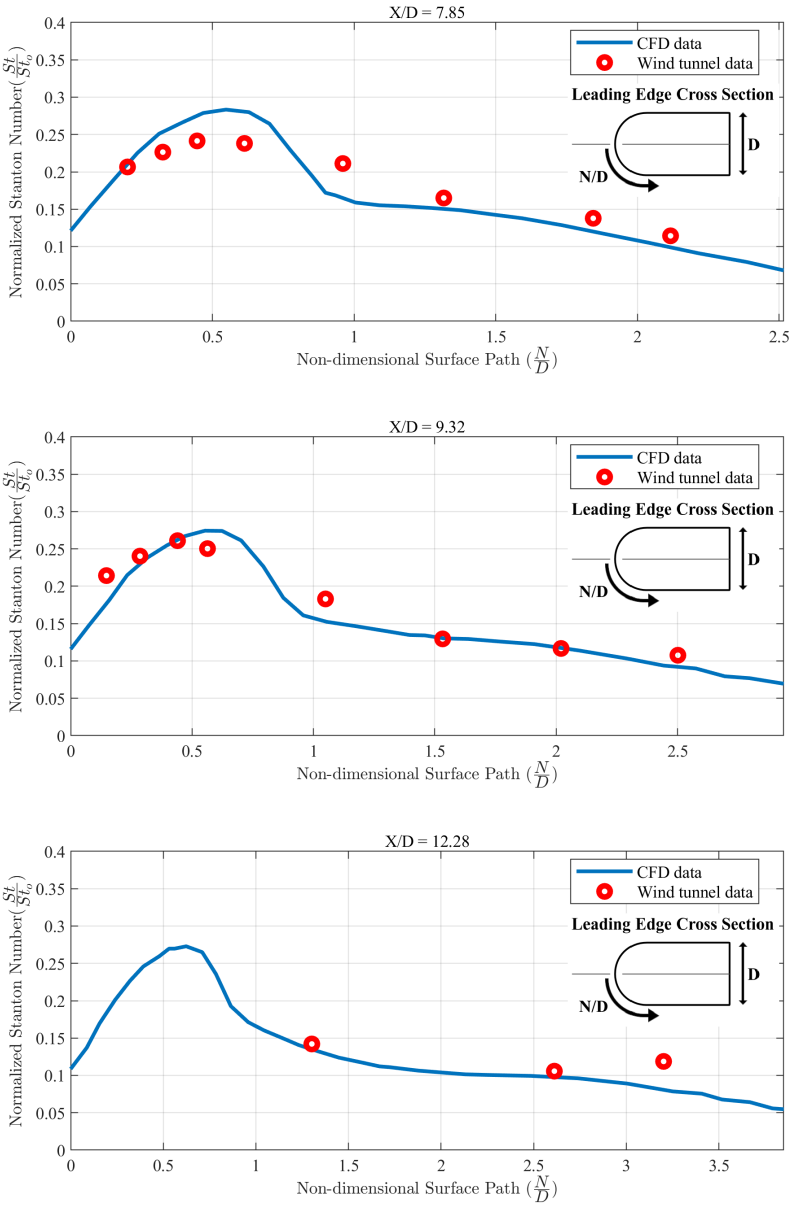

Figure A.13: Normalized Stanton number against non-dimensional surface path for angle of attack 30° at non-dimensional leading edge locations 7.85, 9.32, and 12.28.

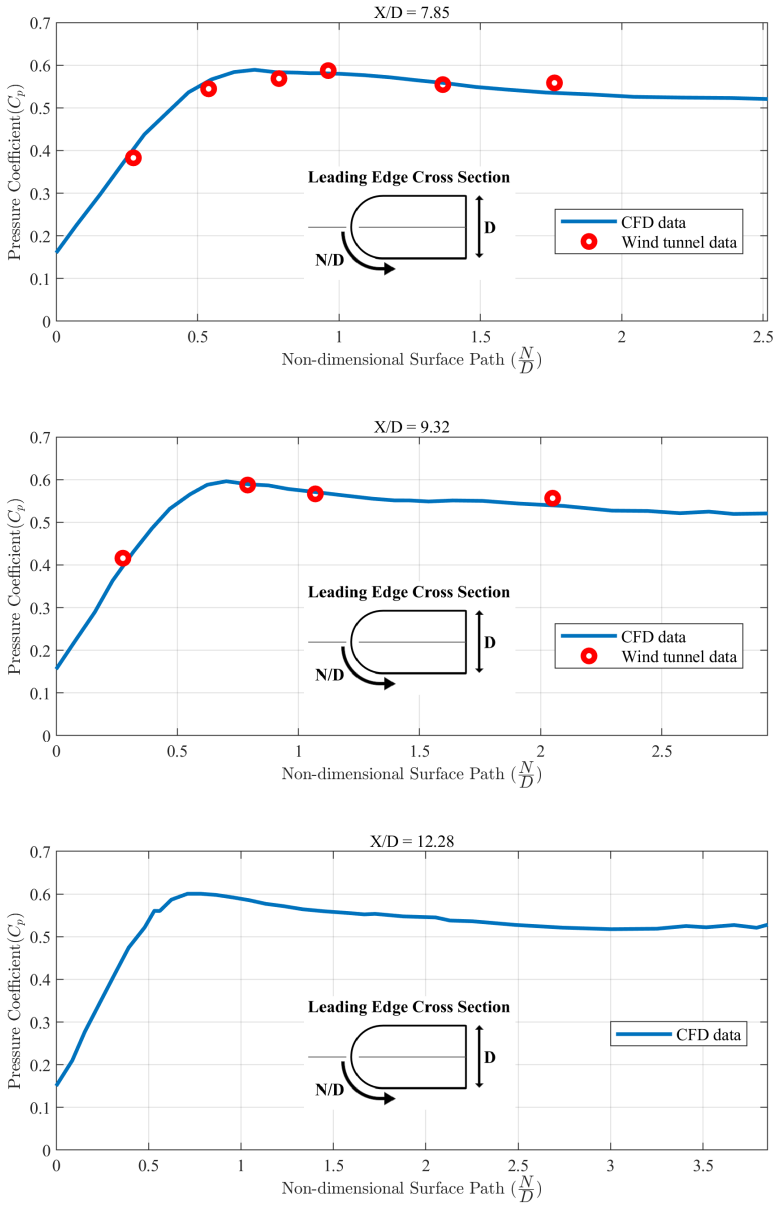

Figure A.14: Pressure coefficient against non-dimensional surface path for angle of attack 30° at non-dimensional leading edge locations 7.85, 9.32, and 12.28.